Truncated radial glia as a common precursor in the late corticogenesis of gyrencephalic mammals

Running title: Binary fates of tRG in corticogenesis

Authors list

Merve Bilgic[1,2,3], Quan Wu[1,4*], Taeko Suetsugu[1,4], Atsunori Shitamukai[1,5], Yuji Tsunekawa[1,6], Tomomi Shimogori[7], Mitsutaka Kadota[8], Osamu Nishimura[8], Shigehiro Kuraku[8,9], Hiroshi Kiyonari[10], and Fumio Matsuzaki[1,2,4*]

Affiliations

[1]Laboratory for Cell Asymmetry, RIKEN Center for Biosystems Dynamics Research, Kobe, Hyogo 650-0047, Japan.

[2]Laboratory of Molecular Cell Biology and Development, Department of Animal Development and Physiology, Graduate School for Biostudies, Kyoto University, Kyoto 606-8501, Japan.

[7]Molecular Mechanisms of Brain Development, RIKEN Center for Brain Science, Wako, 17 Saitama 351-0198, Japan.

[8]Laboratory for Phyloinformatics, RIKEN Center for Biosystems Dynamics Research, Kobe, Hyogo 650-0047, Japan.

[10]Laboratory for Animal Resources and Genetic Engineering, RIKEN Center for Biosystems Dynamics Research, Kobe, Hyogo 650-0047, Japan.

[*]Corresponding authors

go.quan.8w@kyoto-u.ac.jp

matsuzaki.fumio.2w@Kyoto-u.ac.jp

Further information and requests for resources and reagents should be directed to and will be fulfilled by the lead contact, Fumio Matsuzaki (matsuzaki.fumio.2w@Kyoto-u.ac.jp)

[3]Present address: The Institute for Quantitative Biosciences, The University of Tokyo, Tokyo 113-0033, Japan.
[4]Present address: Department of Aging Science and Medicine, Medical Innovation Center, Graduate School of Medicine, Kyoto University, Kyoto 606-8507, Japan.
[5] Present address: Department of Human Morphology, Graduate School of Medicine, Dentistry and Pharmaceutical Sciences, Okayama University, Okayama 700-8558, Japan.
[6]Present address: Division of Molecular and Medical Genetics, Center for Gene and Cell Therapy, The Institute for Medical Science, The University of Tokyo, Tokyo 108-0071, Japan.
[9]Present address: Molecular Life History Laboratory, Department of Genomics and Evolutionary Biology, National Institute of Genetics, Mishima, Shizuoka 411-8540, Japan.

Character count (excluding materials and methods, references, and figure legends): 34742

ABSTRACT

The diversity of neural stem cells is a hallmark of the cerebral cortex development in gyrencephalic mammals, such as Primates and Carnivora. Among them, ferrets are a good model for mechanistic studies. However, information on their neural progenitor cells (NPC), termed radial glia (RG), is limited. Here, we surveyed the temporal series of single-cell transcriptomes of progenitors regarding ferret corticogenesis and, found a conserved diversity and temporal trajectory between human and ferret NPC, despite the large timescale difference. We found truncated RG (tRG) in ferret cortical development, a progenitor subtype previously described in humans. The combination of *in silico* and *in vivo* analyses identified that tRG differentiate into both ependymal and astrogenic cells. Via transcriptomic comparison, we predict that this is also the case in humans. Our findings suggest that tRG plays a role in the formation of adult ventricles, thereby providing the architectural bases for brain expansion.

Keywords:

Single-cell transcriptome / neural stem cell / brain development / ferret / human / neurogenesis / truncated radial glia.

INTRODUCTION

A vast diversity of neurons and glia form functional neural circuits during the development of the cerebral cortex in mammals. These cells are progressively generated from multipotent neural stem cells, termed radial glia (RG), following genetic processes common across species, from initially neurons of the deep layers (DL), then neurons of the upper layers (UL), and finally glial cells, astrocytes, or oligodendrocytes (**Fig. S1A, S1B**; Rowitch and Kriegstein, 2010). These processes are also spatially organized with RG divisions in the ventricular zone (VZ), IPC-neuron differentiation in the sub-VZ (SVZ), and neuron migration to the cortical plate in an inside-out manner. In many mammalian phylogenic states, cerebral cortex evolved to gain an additional germinal layer (outer SVZ, OSVZ; Smart et al, 2002), where extensive neurogenesis and gliogenesis of outer RG (oRG) occur (Hansen *et al*, 2010; Fietz *et al*, 2010; Reillo *et al*, 2011; Gertz & Kriegstein, 2015) resulting in the amplification of neuronal and glial populations in the cortex (**Fig. S1**; Rash et al, 2019). On the other hand, a new subtype of NPC in the VZ has recently been reported in humans and rhesus macaques (deAzevedo et al,

2003; Nowakowski et al, 2016; Sidman and Rakic, 1973), lacking the basal attachment and is therefore termed truncated RG (tRG). However, how widely tRG appears in gyrencephalic (or even lissencephalic) mammal development, what mechanisms underlie their formation, and what they produce remain unknown. As distinct NPC subtypes may possess different capacities to generate differentiated progenies (Huang et al, 2020; Rash et al, 2019), it would be critical to find answers to those questions to understand commonality and diversity in the mammalian brain evolution.

Genetic manipulation of individual cell types *in vivo* and single-cell transcriptome analysis are two major and successful approaches in revealing the properties of cells, such as their proliferation and differentiation. Thus, single-cell RNA sequencing (scRNA-seq) of the human brain during development has been extensively performed (Herring *et al*, 2022; Bhaduri et al, 2020, 2021; Huang et al, 2020; Johnson et al, 2015; Liu et al, 2017; Polioudakis et al, 2019; Pollen et al, 2015; Zhong et al, 2018). However, the *in vivo* behavior in humans and other primates and the underlying mechanisms remain less explored owing to the limited experimental access to the developing primate cortices. Particularly, resources available for the late human embryonic brain are extremely rare due to ethical challenges. Also, studies using brain organoids face issues in recapitulating the specification and maturation of cell types during human brain development (Bhaduri et al, 2020). In this context, the ferret (*Mustela putorius furo*) is highlighted as a suitable animal model, which compensates for the difficulties in studying human cortical development. Ferrets are carnivores that develop common gyrencephalic features, such as the OSVZ and a folded brain, and are frequently used in mammalian models of brain development and circuit formation because neurogenesis continues in their early neonatal stages (Chapman & Stryker, 1992; McConnell, 1988; Noctor *et al*, 1997; Jackson *et al*, 1989). Since this species is experimentally manipulable, recent studies have developed *in vivo* gene manipulation and editing technology using *in utero* electroporation (IUE; Matsui et al, 2013; Kawasaki et al, 2012; Tsunekawa et al, 2016; timelapse imaging; McConnell, 1995; Chenn & McConnell, 1995). Furthermore, ferrets showed severe microcephalic phenotypes via *ASPM* (*Abnormal Spindle-like Microcephaly-associated* gene) knockout (Johnson et al, 2018; Kou et al, 2015), which greatly differs from a minor phenotype in mouse *ASPM* knockout mutants (Capecchi and Pozner, 2015; Fujimori et al, 2014; Jayaraman et al, 2016; Pulvers et al, 2010). This remarkable finding suggests the presence of mechanisms underlying brain enlargement and circuit complexity shared by gyrencephalic species to some extent. Results from transcriptome profiling of ferret cortical

96 cells has revealed regional differences in germinal layers and cell-type composition (Johnson
97 et al, 2018; de Juan Romero et al, 2015). However, because of the incomplete genomic
98 information, especially due to the lack of genetic models, the databases with ferret data have
99 been less reliable than those with human or mice data. This has posed a limit for the accurate
100 comparison of single cell transcriptomes between ferrets and humans. Hence, the temporal
101 pattern of molecular signatures of ferret NPC remains largely unexplored at single-cell
102 resolution. Comparison of progenitor subtypes and sequential events at the single-cell
103 transcriptome level regarding development between ferrets and humans will greatly help to
104 recognize common and species-specific mechanisms underlying the construction of a complex
105 brain.
106
107 In this study, we comprehensively analyzed the developmental dynamics of progenitor
108 populations during ferret corticogenesis to clarify shared or species-specific mechanisms of
109 corticogenesis in gyrencephalic mammals and found that ferrets generate tRG at late
110 neurogenic and early gliogenic stages like humans and other primates. Analysis of the
111 pseudotime trajectory and temporal histochemical pattern suggested that tRG generate
112 ependymal and astrogenic cell fates. Then, we compared temporal series of ferret and human
113 single cell transcriptomes (Bhaduri et al, 2021; Nowakowski et al, 2017). Remarkably, we
114 found homologous temporal progenitor trajectories irrespective of the large differential
115 corticogenesis timescale. This study combining rich ferret and human transcriptome data with
116 *in vivo* analysis using ferrets emphasizes the value of single-cell ferret transcriptome datasets.
117
118 **RESULTS**
119 **Temporal patterns of neurogenesis and gliogenesis in the cerebral cortex of ferrets**
120 First, we confirmed histochemically the spatial and temporal pattern of RG, oRG, and IPC and
121 the appearance of diverse cortical neurons to determine the period in which samples were to
122 be taken for scRNA-seq (**Fig. S1**). While neurogenesis mostly terminated by P5 in the dorsal
123 cortex (**Fig. S1A, S1B**), oligodendrocyte progenitors of dorsal origin ($OLIG2^+$) and RG with
124 gliogenic potential ($GFAP^+$) became detectable approximately at E40 and increased in number
125 postnatally (**Fig. S1C, S1D**). To recapitulate neurogenesis and gliogenesis in the ferret cortex
126 at a high resolution, we decided to determine the temporal trajectories of cell types in the course
127 of ferret brain development (schematically represented in **Fig. 1A**) by performing single cell
128 transcriptomes of neural progenitors, neurons and glial cells. Based on the above histochemical

observations (**Fig. S1A, S1B**), we examined single cell transcriptomes at the six developmental time points: embryonic days E25, E34, and E40 and postnatal days P5 and P10. We carried out single-cell RNA-sequencing (scRNA-seq) of ferret dorsal cortex at these six developmental time points (**Fig. 1**). We prepared two series of cell populations isolated in different ways to enrich the progenitor subtypes (**Fig. 1B**): (1) FACS-based sorting of the neural stem cell fraction labeled with an AzamiGreen (AG)-driven *HES5* promoter (Ohtsuka et al, 2006) and (2) collecting cells forming the VZ, SVZ, and intermediate zones (IZ) of cerebral cortices after discarding the cortical plate (CP, **Fig. 1B, S2A**).

Improvement of the gene model for scRNA-seq of ferrets

High quality information about gene models over the entire genome is prerequisite to obtain a high resolution of single cell transcriptomes from scRNA-seq. Despite several previous transcriptome studies on the ferret cortex (Johnson et al, 2018; de Juan Romero et al, 2015), public information on the ferret genome is incomplete; identification of the gene corresponding to a cDNA requires its accurate 3'-untranslated region (3'-UTR) and its correct connection to the coding sequence, because single cell-cDNA library were made by Oligo (dT)-priming method (10x Genomics Chromium, **Fig 1C)**. However, information regarding the 3′-UTR of genes had been poor for ferret genomic datasets, which has impeded high resolution single-cell transcriptome analyses that can offer an accurate comparison with human datasets, Thus, we first improved the annotations of ferret genomic DNA sequences using Chromium droplet sequencing, which tagged all contigs from a long genomic DNA in a droplet, and constructed new gene models based on the improved genomic annotations and newly obtained RNA-seq reads of various tissue types (**Table S7 and see Materials and Methods**). Comparing with NCBI references, mapping scRNA-seq reads from E34 to our own references not only improved the mapping rate (number of reads mapped to the transcriptome) from ~30% to ~56%, but also increased the median number of genes detected from ~1000 to ~2000. (**Fig. 1D**). We found similar mapping rate and median number of genes detected across all sampling stages (**Table S1**).

Single-cell RNA-seq revealed subtypes of cortical cells in ferrets

We then combined scRNA-seq information from the two cell populations on all the sampling stages for unbiased clustering. **Fig. 2A** shows cell clustering projected in the Uniform Manifold Approximation and Projection (UMAP) space (preprint: McInnes et al, 2018; Stuart et al, 2019). We characterized 26 transcriptionally distinct clusters from 30,234 ferret cortical cells through

163 corticogenesis and detected up to 2,600 median genes per cell (**Fig. 1D, E; Table S1**). After
164 combined clustering of the two collectives of cell populations prepared by independent
165 methods, we re-separated cells into each collective, and confirmed a reproducibility of
166 clustering between two different collectives (**Fig. S2B**).
167
168 We also examined whether cells with high mitochondrial contents affect clustering of ferret
169 single cells, because we have decided to include all cells that had less than 30% of
170 mitochondrial genes in our analysis based on the percentage of reads mapped on the
171 mitochondrial genome; we found that the majority of cells in each cell type had a value less
172 than 5% while some cells contained them in the range between 0% and 10%, up to a maximum
173 of 28% (**Fig, 1E**). We confirmed that single cells after filtering cells with the threshold of 10%
174 mitochondrial content (28,686 cells in our dataset) and those with the threshold of 30% (**Fig.**
175 **2A**), provided similar clustering patterns with each other, both of which 26 clusters **(Fig. S2C)**
176 indicating that the current selection of cells with the mitochondrial contents is appropriate.
177
178 Cell clusters were annotated according to their specific gene expression patterns (**Fig. 2B, C,**
179 **S3A, Table S1**) and assigned into ten cell types: RG (early, mid, and late), IPC, OPC,
180 ependymal cells, excitatory cortical neurons (DL and UL), inhibitory neurons (ITN), microglia,
181 endothelial cells, mural cells, and unknown cells (**Fig. 2A**). RG, IPC, and neuronal clusters
182 were aligned according to the neuronal differentiation process in the UMAP plot (**Fig. 2A**). RG
183 cells were classified into three clusters (early, mid, and late) according to their collection stages
184 and also the expression of temporally altered RG markers reported previously (hereafter named
185 temporal markers) (Okamoto et al, 2016; Telley *et al*, 2019). The "early RG" clusters
186 comprised E25 cells while the "mid RG" clusters, mostly E34 cells (**Fig. S3B**). Early and late
187 RG, and IPC were subdivided into three subclusters that expressed different cell cycle markers
188 (**Fig. S3C**).
189
190 Remarkably, we identified a small cluster (409 cells) of *PAX6*-expressing RG subtype, 69% of
191 which expressed *CRYAB* (**Fig. 2D**). *CRYAB*, encoding a molecular chaperone (Yamamoto et
192 al, 2014) is a unique marker for human tRG (Nowakowski et al, 2016); therefore, we designated
193 them as tRG-like cells in ferrets. In contrast, oRG cells failed to be distinguished from
194 ventricular RG cells (vRG) in ferrets by unbiased clustering alone (see below). HOPX, a typical
195 marker for oRG in human tissues (**Fig. 2E, S3D**; Pollen et al, 2015), has been indeed detected

196 in both oRG and vRG at late stages *in vivo* in ferrets (**Fig. S3D**; Johnson et al, 2018; Kawaue
197 et al, 2019).
198
199 **tRG emerge around birth during the development of somatosensory cortex in ferrets**
200 The presence of a tRG-like cluster in ferret transcriptomes led us to investigate the properties
201 of the cells in this cluster. To examine their cell morphology, we sparsely labeled NPC by
202 electroporating P0 embryos with an expression vector for enhanced green fluorescent protein
203 (EGFP) and found a cell population showing major characteristics of human tRG cells
204 (Nowakowski et al, 2016): expression of CRYAB and PAX6 with an apical endfoot and
205 truncated basal fiber in the VZ during late neurogenesis (**Fig. 3A,B, Supplementary movie1,**
206 **2**). CRYAB expression emerged shortly prior to birth (day 41), gradually increasing in cell
207 number, and became mostly restricted to tRG-shaped cells in the VZ and SVZ (**Fig. 3C, 3D,**
208 **S4A**). These CRYAB^{+} cells were mostly post-mitotic (KI67^{-}) and neither IPC (TBR2^{+}) nor
209 OPC (OLIG2^{+}) at P10, while a small fraction of those cells expressed these markers at P5 (**Fig.**
210 **3E–3G**). These histochemical observations were consistent with our single-cell transcriptome
211 data (**Fig. S4A–F**). Altogether, we concluded that tRG-like cells in ferrets are equivalent to
212 human tRG cells (as also confirmed by transcriptomic comparison between humans and ferrets,
213 shown later). A difference in the late neurogenic cortex between humans and ferrets is that the
214 VZ and OSVZ are connected by conventional RG cells in ferrets (**Fig. 3A, S4G**), but separated
215 in humans due to the disappearance of conventional RG cells (Nowakowski et al, 2016).
216
217 **Temporal fates of RG cells are predicted by pseudo-time trajectory analysis**
218 To understand the relationship between various cortical progenitors in the developing ferret
219 brain, particularly in the origin and fate of ferret tRG, pseudo-time trajectory analysis was
220 performed. Single cells that had been subjected to single-cell transcriptome analyses (from E25
221 to P10) were unbiasedly ordered along a trajectory based on their transcriptome profiles (**Fig.**
222 **S5A, S5B**). To simplify our analysis, we first excluded interneurons, microglia, endothelial
223 cells, and excitatory neuronal clusters. Subsequently, 6,000 single cells were randomly selected
224 from the remaining cell population for further analysis. The pseudo-time analysis predicted a
225 reasonable trajectory consisting of three branching points that generated seven states (**Fig. 4A,**
226 **S5B**). We assigned major cell types for each state based on the cell clusters defined by UMAP
227 analysis (**Fig. 3A, Table S2**). The trajectory successfully predicted cortical development, along
228 which *HES1*$^{+}$ stem cells shift their features from the earlier to the later stages, generating

229 branches of differentiated cells (**Fig. 4B, 4C, S5D**). Major *HES1*$^{+}$stem cell states (state 1, 3, 5
230 and 7) contained cells at different stages; thus, termed NPC1, 2, 3 and astrogenic, respectively
231 (**Fig. S5C**). NPC1 (mostly from E25) bifurcated into the neuronally differentiated lineage and
232 NPC2 state (**Fig. S5B**), which produced the OPC lineage and NPC3 state at the second
233 branching point. When neurogenesis gradually declined after birth, the NPC3 state, mainly
234 consisting of late RG cells and tRG (**Fig. S5C**), adopted two states, state 6 with an presumptive
235 ependymal fate (*FOXJ1*$^{+}$, *SPARCL1*$^{+}$) and state 7 with presumptive astrogenic fate (*FOXJ1*$^{-}$,
236 *SPARCL1*$^{+}$), as judged by the combination of late fate markers (Liu et al, 2022; Saadoun and
237 Papadopoulos, 2010; Yu et al, 2008, **Fig. S3A, 3D**).
238
239 Remarkably, tRG cell population was distributed into three branches along the pseudo-time
240 trajectory (**Fig. 4D, 4F**): NPC3 (mainly during E40–P1), astrogenic (P1–P10), and ependymal
241 (P5–P10) branches, suggesting that tRG prenatally arise as precursors of ependyma and
242 astroglia in the ferret cortex (see below). Different territories were assigned into these three
243 states in the UMAP even when we examined the entire tRG population (409 cells) before
244 making a random selection of 6,000 cells for pseudotime trajectory analysis, supporting the
245 reliability of this presumptive categorization of tRG (**Fig. 4E**).
246
247 **tRG cells is likely to possess ependymal and gliogenic potential during cortical**
248 **development in ferrets**
249 To test the hypothesis that tRG generate both ependymal cells and astroglia populations, we
250 first examined the expression of an ependymal marker, FOXJ1, a master regulator of
251 ciliogenesis, according to CRYAB expression in the VZ. We observed that CRYAB^{+} tRG
252 cells gradually co-expressed FOXJ1, reaching up to 90% co-expression by P10 (**Fig. 5A,**
253 **5B**). Similarly, our transcriptome data showed that the fraction of *CRYAB-FOXJ1* double-
254 positive cells increased in the tRG cluster from P1 to P10, whereas other RG clusters
255 maintained low *CRYAB* expression (**Fig. 5C, 5D**). From P5 onwards, differentiating
256 ependymal cells (*CRYAB-FOXJ1* double-positive) accumulated within the VZ (**Fig. 5A**).
257 These cells often align their nuclei in parallel to the ventricular surface, near which nuclear
258 lined aggregates are observed more frequently (between two arrowheads in P5 and P10 in
259 **Fig. 5A**), and their cell body finally settled on the apical surface with short basal fibers by
260 P14 (**Fig. 5E**). These data suggest that a majority of tRG cells progressively upregulates
261 *FOXJ1* expression to adopt an ependymal cell fate during postnatal development.

262 Concomitantly, adenine cyclase III expression in both primary and multiciliated cells
263 indicated that ciliogenesis progressed postnatally, forming multi-ciliated ependymal cells on
264 the ventricular surface of the ferret cortex by P35 (**Fig. S6A**). Altogether, it is most likely
265 that FOXJ1^{+}tRG are fated to be ependymal cells that constitute the ventricular surface. To
266 prove this, it is necessary to chase tRG by knocking in a fluorescent marker gene via *in utero*
267 electroporation, or to follow the change in cell shape from tRG to a characteristic ependymal
268 morphology in slice cultures by labeling with a fluorescent gene via *in utero* electroporation.
269 However, the latter would not be realistic, because the process of the transformation from
270 tRG to ependymal cells is slow to take a long time in an order of 10 days. It is an important
271 future issue to develop the strategy to genetically follow the fate of tRG.
272
273 Moreover, a fraction of tRG belongs to the state 7 (astrogenic state) in the pseudo-time
274 trajectory (**Fig. 4E, 4F**). We examined whether these tRG cells differentiate into astrogenic
275 cells. We chose *FOXJ1* as an ependymal marker and *SPARCL1* as an early astroglial marker
276 based on a recent study in mice (Liu *et al*, 2022). While *SPARCL1* is expressed in all states
277 generated by NPC2 (**Fig. S6B**), *SPARCL1* expression is highest in astrogenic tRG among the
278 three tRG subgroups, whereas *FOXJ1* expression is nearly exclusive to ependymal tRG (**Fig.
279 4F**). Furthermore, cells expressing high levels of *SPARCL1* do not express *FOXJ1* (**Fig. 4G,
280 Table S3**). These features of the astrogenic tRG are essentially the same as those of the
281 astrogenic state (state 7) of the pseudo-time trajectory (**Fig. 4D**). Consistently, whereas
282 FOXJ1^{+} cells were located close to the apical surface, those expressing *SPARCL1* were
283 observed relatively far from the apical surface in the VZ (**Fig. 5H, 5I, S6C, Table S4**). Taken
284 together, our analyses strongly suggest that tRG cells adopt both the ependymal and astroglial
285 fates.
286
287 **Ferrets and humans show a homologous developmental transcriptomic profile of
288 progenitor subtypes**
289 Both ferrets and humans are positioned in distinct phylogenetic branches; both represent
290 complex brain features of gyrencephalic mammals. Therefore, we compared our temporal
291 series of ferret single-cell transcriptomes with a previously published human dataset
292 (Nowakowski et al, 2017) to examine which processes are species-specific or common for the
293 two species. We merged the two datasets by pairing mutual nearest neighbor cells (MNN)
294 following canonical correlation analysis (CCA) across species (Stuart and Butler et al, 2019)
295 and found that many cell types, including RG, IPC, OPC, and neurons, were clustered together

296 (**Fig. 6A, S7A**). Temporal patterns and variety of neural progenitors during cortical
297 developments were similar to each other between humans and ferrets at the single cell
298 transcriptome level. Nonetheless, the timescales of cortical development significantly differed:
299 on the UMAP plot, ferret E25 cells closely distributed with human GW8 cells; ferret E34, with
300 human GW11–14; ferret E40–P1, with human GW15–16; and ferret P5–P10, with human
301 GW17–22 (**Fig. 6B**).
302
303 Next, we compared the similarities among individual RG subtypes across species. To quantify
304 the features of an RG subtype, we introduced the parameter "genescore" (Bhaduri et al, 2020),
305 a parameter that reflects the enrichment and specificity of a marker gene for a given cluster;
306 the genescore for a particular marker gene is defined by multiplying the average enrichment of
307 expression quantity in cells of the cluster (fold change) and the ratio of the number of marker-
308 expressing cells in the cluster to the cell number in all other clusters (see **Materials and**
309 **Methods**). Comparison of genescores of two arbitrary RG subtypes between two species
310 revealed a high correlation in the early and late RG clusters (vRG, and oRG for the human
311 dataset) across species (**Fig. 6C, 6D, Table S5**).
312
313 tRG cells also showed a remarkable similarity between the two species (**Fig. 6C, 6D**), as
314 represented by a high level of expression for the combination of *CRYAB*, *EGR1,* and *CYR61*
315 (**Fig. 6E**). To better examine this similarity, we defined the "cluster score" for individual cells
316 as a linear combination of the expression level of marker genes in a cell, which is weighted by
317 its genescore in the human cluster of interest. Calculation of the cluster score for ferret tRG
318 using genescores of the human tRG cluster resulted in a higher score than any other cluster in
319 both datasets (**Fig. 6F**). These results confirm, via transcriptomics, that the ferret tRG cluster
320 is very close to the human one.
321
322 **Transcriptional analysis of human tRG subtypes by integration with ferret tRG subtypes**
323 Next, we assessed whether human tRG cells also possessed ependymal and gliogenic potential,
324 as suggested in ferret cells. We chose a recently published human dataset (Bhaduri et al, 2021)
325 for comparison**,** because this study containing GW25 dataset which included more tRG cells
326 than previous studies that did not contain GW25 data. Furthermore, we used only data at
327 GW25. After excluding neurons and other cell types from the analysis, we identified respective
328 human clusters for tRG and oRG cells based on their marker gene expression (**Fig. 7A, Table**

329 **S6).** Then, we merged this human dataset and ferret NPCs (**Fig. 7B, 7C**) by the MNN after
330 CCA as described before when we merged the entire series of progenitor samples of ferrets
331 and humans (**Fig. 6A)**. This procedure revealed that human tRG and oRG share similar
332 transcriptomes with ferret tRG and late RG that must include oRG, respectively (**Fig. 7D-H**
333 **and Fig. S8A, S8B**). It is worth noting that early RG in ferrets showed the highest similarity
334 with "OLIG1" in human data, and no cell type in human data corresponded to ferret "midRG,"
335 likely because only GW25 cells were used for comparison (**Fig. S8A, S8B**).
336
337 The integration of ferret and human datasets showed that tRG from both species were mainly
338 distributed into three different clusters in the UMAP space: 7, 21, and 28 (**Fig. 7F, S8C**).
339 Cluster 7 cells highly expressed late onset RG genes (such as *APOE*, *FABP7*, *NOTCH2*, and
340 *DBI*; **Fig. S8D**), suggesting that tRG cells in cluster 7 were presumably at a late RG-like state,
341 being not yet committed to neither astrogenic nor ependymal fates (mostly in the NPC 3 state
342 in the ferret pseudo-time trajectory; **Fig 3A, 3E**). In contrast, cells in clusters 21 and 28 highly
343 expressed marker genes for the astrocyte (*GFAP* and *AQP4*), and the ependymal (*FOXJ*1)
344 clusters, respectively (**Fig. S8D, Table S6**). Then, we confirmed that the three states of ferret
345 tRG cells, committed to the astroglia, ependymal fates and uncommitted states, were largely
346 assigned to clusters 21, 28 and 7, respectively (**Fig. 7G**), guaranteeing the reliability of this
347 method. Thus, our results raise the possibility that tRG cells in humans possess the potential to
348 generate astrocytes and ependymal cells as suggested for ferret tRG. This analysis also reveals
349 that the proportion of the 3 tRG subtypes was very different between human and ferret datasets
350 (**Fig. S7D–F**); the two presumptively committed tRG are very minor populations in humans,
351 possibly due to the differences in developmental stages where tRG of these subtypes are
352 enriched (see Discussion).
353
354 **Human cortical organoids lack tRG population**
355 Human cortical organoids are a powerful model for understanding cortical development
356 (Eiraku *et al*, 2008). It is, therefore, important to know how developing ferret cortices resemble
357 human cortical organoids especially regarding to features shared by human tissues and ferrets.
358 We then decided to analyze two different datasets of cortical organoids to see whether tRG is
359 present in those organoids (**Fig. S9A-D** for Bhaduri et al., 2020; **Fig. S9E-F** for Herring et al.,
360 2022), by focusing on CRYAB-expressing cells (**Fig. S9**). We assigned cells according to the
361 original annotations, which included the information of organoid lines, age, and state (**Fig.**

362 **S9A**). Our clustering resulted in 32 clusters where CRYAB-expressing cells were detected in
363 two out of four cell lines (**Fig. S9B**). We noted that a tRG cluster was absent in the original
364 annotation. To further confirm the absence of a tRG cluster in organoids, we integrated
365 organoid dataset with the dataset derived from human primary tissues (Bhaduri et al., 2020).
366 After the integration, we failed to find organoid-derived CRYAB-expressing cells that
367 overlapped with tRG cells from the human primary tissues (Bhaduri et al., 2020; **Fig. S9C-D**),
368 nor CRYAB-expressing cell itself in the other dataset (Herring et al., 2022; **Fig. S9E**). Our
369 analyses thus indicate that tRG-like populations seem to be lacking in organoid datasets that
370 are currently available (Bhaduri et al., 2020, Herring et al., 2022).
371

372 **Prediction of ferret oRG-like cells via the identification of cells homologous to human**
373 **oRG cells**

374 As mentioned before, oRG could not be identified as a separate cluster in the ferret dataset (**Fig.**
375 **1**). We attempted to assign oRG-like cells in the ferret dataset using human oRG cells as
376 anchors via the integration of two datasets by the MNN after CCA (**Fig. 7B**). We could assign
377 oRG-like cells, which were located near the human oRG cluster (**Fig. 7H**). To assess the degree
378 of similarity to human oRG, we calculated the oRG score for each ferret oRG-like cell as we
379 did for tRG (**Fig. 6F**). The assigned oRG-like cells had significantly higher oRG cluster scores
380 than all other NPCs (**Fig. 7I**). Furthermore, we searched genes that were highly expressed in
381 oRG-like cells by comparing oRG-like cells and other NPCs in the ferret dataset (**Table S6**).
382 Consistent with the human dataset (Bhaduri *et al*, 2021), the expression of *HOPX, CLU,* and
383 *CRYM* was higher in oRG-like cells than in other ferret NPCs (**Fig. 7J, S8E**). However, human
384 oRG markers such as *HOPX* and *CLU* were also expressed by vRG and tRG in ferrets (**Fig.**
385 **S3D, S8F**). Therefore, oRG at the transcriptome level can only be distinguished by the
386 similarity with the whole transcriptome or a combination of several markers, but not by a few
387 marker genes, whereas oRG can be unambiguously identified by its location in the tissue (**Fig.**
388 **S1**).
389

390 **DISCUSSION**

391 In this study, we provide a ferret dataset of single-cell transcriptomes of neural progenitors
392 covering the entire cortical neurogenenesis and early gliogenic phase, revealing their diversity
393 and temporal patterns during cortical development. Comparison of these features between
394 ferrets and humans (Nowakowski *et al*, 2017; Bhaduri *et al*, 2021) indicated at a high resolution
395 that these two gyrencephalic mammals shared a large proportion of progenitor variations and

396 their temporal sequences despite their extremely different neurogenesis timescales. It is
397 remarkable that tRG is conserved between these two phylogenetically distant species. A ferret
398 model allows us to identify the mode of tRG generation, to predict its descendant fates and to
399 analyze cell dynamics in tissues. These findings have not been realized by previous studies, re-
400 evaluating ferrets as a valuable model species to study the neural development of gyrencephalic
401 animals. This comparison between humans and ferrets could not be performed unless genomic
402 information, especially genome-wide gene models, was greatly improved; there had been
403 sufficient genomic information accumulated for ferrets, but mainly for coding regions for genes,
404 which had not been well connected to their 3'-UTR. However, to carry out a large scale of
405 single cell RNA seq quantitatively with minimizing the loss of transcript species, accurate 3'-
406 UTR sequences and their link to the coding part are indispensable, because typical scRNA-seq
407 platforms are based on oligo-(dT)-primed cDNA synthesis. We made tremendous efforts to get
408 improved gene models that include 3'-UTR sequences, making it possible for us to compare
409 single cell transcriptome of ferret cortical progenitors with a huge volume of single cell
410 transcriptome datasets with high qualities, including those for humans and mice.
411
412 **The fate of tRG progenies**
413 Our pseudotime trajectory analyses and immunohistochemistry analyses suggested that ferret
414 tRG cells differentiate into ependymal cells and astrogenic cells. Although the number tRG
415 cells used in the trajectory analysis was limited (167 cells; **Fig. 3**), three tRG subtypes, which
416 are presumably "precommitted", "ependymal" and "astrogenic" tRG also formed three distinct
417 territories within the original tRG cluster that consisted of 409 cells on UMAP, indicating a
418 consistent heterogeneity within tRG cluster. This mode of the presumptive ependymal cell
419 formation is likely parallel to that of the bifurcation of ependymal cells and adult neural stem
420 cells from the same progenitor population in the striatum on the ventral side (Ortiz-Álvarez *et*
421 *al*, 2019).
422
423 **Comparison of human with ferrets in corticogenesis**
424 Our cross-species comparative analysis predicts that tRG in humans also differentiate into
425 ependymal and astroglial cells although there is no *in vivo* evidence yet (**Fig. 6E**). Furthermore,
426 the rare presence of two presumptively committed tRG subgroups in humans makes this
427 prediction tentative at present. If this prediction is the case, the uncommitted tRG fraction is
428 dominant in GW25 human brains unlike in ferret brains, suggesting that human tRG at GW25

429 progresses along the differentiation axis less than ferret tRG at P5–P10, most of which are
430 already committed to either ependymal or astrogenic states.
431 While GW25 has been almost at the latest stages experimentally available from human
432 embryonic brain tissues due to ethical reasons, Herring et al. recently reported a large dataset
433 that spans late embryonic to postnatal development in human prefrontal cortex, in which we
434 were not able to detect a tRG population nor other progenitor subtypes, as well as an ependymal
435 cell type (Herring *et al*, 2022), possibly due to regional differences in the collected samples
436 from our ferret dataset. Thus, this postnatal dataset does not seem to be appropriate to compare
437 with our ferret dataset or even human prenatal dataset (Bhaduri et al. 2020) to follow tRG
438 progenies (**Fig. S9**). More enrichment of datasets in the human lateral cortices at the
439 developmental stages after GW25 onward are necessary to test whether our results obtained
440 from ferrets regarding tRG progeny fates can be generalized.
441
442 **Commonalities and differences among characteristics of neural progenitors between**
443 **human ferrets.**
444 In this study, our transcriptomic data supported the notion that ferrets are a good model
445 system to investigate mechanisms commonly (at least in both primates and carnivores)
446 underlying the cortical development in gyrencephalic mammals. At the same time, we
447 acknowledge the differences in corticogenesis between ferrets and humans. Most prominently,
448 the time scale of corticogenesis progression is greatly different between the two species, while
449 the variety of NPCs and their temporal patterns of appearances and differentiation exhibit
450 similarities. In addition, the organization of cortical scaffold seems differ from each other; in
451 human corticogenesis, two major germinal layers, the VZ and OSVZ, become segregated
452 during the expansion phase of RG in the neurogenic stage, due to the loss of vRG, which extend
453 from the ventricular surface to the laminar surface, passing through the OSVZ (Nowakowski
454 *et al*, 2016). In contrast, ferrets maintain vRG with a long radial fiber in the VZ alongside with
455 tRG cells, even beyond the expansion phase of tRG (**Figure 3A, S4G**).
456
457 **Models as human cortical development**
458 Our preliminary analysis of two datasets from human cortical organoids suggests the lack
459 of tRG-like cells and potentially their progeny cell types (**Fig. S9**, Bhaduri et al., 2020; Herring
460 et al., 2022). This situation might be improved by optimizing culture protocols. If tRG and
461 ependymal cells, one of the presumptive tRG progeny, are generated in human organoids, as
462 we found in ferrets, it would represent a significant advancement in the human organoid model

463 because ependyma are a fundamental structure for ventricular formation. Further studies using
464 human cortical organoids are expected to be able to generate tRG, and to examine its progeny
465 fates.
466 In ferrets, genetic manipulations can be achieved through *in utero* or postnatal
467 electroporation, as well as via virus-mediated transfer of DNA (Borrell, 2010; Kawasaki *et al*,
468 2012; Matsui *et al*, 2013; Tsunekawa *et al*, 2016). Thus, it is theoretically possible to disrupt
469 the *CRYAB* gene *in vivo* in ferrets to investigate its role in tRG and their progeny, including
470 ependymal cells, and to track the tRG lineage. If the *CRYAB* gene is essential to form
471 ependymal layers, we will be able to explore how the ventricle contributes to cortical folding
472 and expansion. Despite our extensive efforts over a year, we have thus far been unsuccessful
473 in knocking in and/or knocking out the *CRYAB* gene. Nevertheless, we anticipate that technical
474 advances will surpass our expectations, both in ferret and human organoids. Taken together,
475 these functional studies in ferrets as well as in human organoids hold promising insights into
476 the understanding of the tRG lineage and its contribution to cortical development in the near
477 future.
478
479 **MATERIALS AND METHODS**
480
481 **EXPERIMENTAL MODEL AND SUBJECT DETAILS**
482 **Ferret brain tissue samples**
483 Pregnant ferrets were purchased from Marshall BioResources. We also bred them to maintain
484 a population that is sufficient to regularly get pregnant females in the animal facility of RIKEN
485 Center for Biosystems Dynamics Research under the license given from Marshall
486 BioResources. All procedures during animal experiments were performed in accordance with
487 the legal and institutional ethical regulations of RIKEN Center for Biosystems Dynamics
488 Research.
489 Ferret pups are born at day 41 or day 42 of gestation. The day of birth was counted as postnatal
490 day 0 (P0). Ferret embryos and pups were euthanized prior to brain removal.
491 Samples used for single cell RNA-sequencing were obtained from 1 or 2 pups for each
492 developmental stage: embryonic days 25, 34 and 40 and postnatal days 1, 5 and 10. Samples
493 used for immunohistology-based quantifications were obtained from 2 or 3 pups from different
494 mothers. Samples used for a time-lapse imaging were obtained from 1 animal per experiment,
495 which is performed 4 times, independently.
496

497

498 **METHOD DETAILS**

499 **Gene model construction of the ferret genome**

500 In this study, we used a ferret genome reference with expanded reference gene annotations with
501 DDBJ (detail see below). Briefly, gene models were constructed using Chromium by tagging
502 all fragments from a long genomic DNA in a droplet, so that sequences from long genomic
503 DNAs could be successfully aligned to cover so far unconnected genomic regions in the NCBI
504 (NCBI Assembly ID: 286418 (MusPutFur1.0)) database. Detailed information after mapping
505 is listed in the **Supplementary Table S1B**.

506

507 <u>RNA-seq library preparation and sequencing</u>

508 Total RNA was extracted from the embryonic tissues (Supplementary Table S7) using the
509 RNeasy mini kit (Qiagen). Concentration and length distribution of the RNA were checked
510 with the Qubit RNA HS Assay Kit on a Qubit 2.0 Fluorometer (Thermo Fisher Scientific) and
511 the RNA 6000 Nano Kit on a 2100 Bioanalyzer (Agilent Technologies). Sequencing libraries
512 were prepared using 1 μg of total RNA with the TruSeq Stranded mRNA Sample Prep Kit
513 (Illumina) and the TruSeq single-index adaptor (Illumina), except for the sample 'gonad and
514 mesonephros' (see Supplementary Table S7) for which 500 ng of total RNA was used. The
515 RNA was fragmented at 94°C for either 8 minutes or 2 minutes, which resulted in libraries
516 with variable insert size distributions (Hara *et al*, 2015). The optimal numbers of PCR cycles
517 were pre-determined using the KAPA Real-Time Library Amplification Kit (Roche) as
518 described previously (Tanegashima *et al*, 2018). Libraries were sequenced with the Rapid Run
519 mode of HiSeq1500 (Illumina) using the HiSeq PE Rapid Cluster Kit ver. 2 (Illumina) and the
520 HiSeq Rapid SBS Kit v2-HS (Illumina) to produce paired-end reads of 127 nucleotides. Base
521 calling was performed with RTA ver. 1.18.64, and the fastq files were generated with bcl2fastq
522 ver. 1.8.4 (Illumina).

523

524 <u>Genomic DNA extraction and Chromium genome library construction</u>

525 Genomic DNA was extracted from a liver of an adult female ferret using the CHEF Mammalian
526 Genomic DNA Plug Kit (BioRad, Cat. No. #1703591). In brief, the liver tissue of about 50 mg
527 was homogenized in PBS (-) with a Dounce tissue grinder on ice, fixed with ethanol, and
528 subsequently embedded in low melting point agarose gel (BioRad). After the protein digestion
529 with Proteinase K (QIAGEN, Cat. No. #158920) and RNA digestion with RNase A (QIAGEN,
530 Cat. No. #158924), the gel plugs were further digested by Agarase (Life Technologies, Cat.

531 No. #EO0461). DNA was purified by the drop dialysis method using the MF-Millipore
532 Membrane Filter (Merck Millipore, Cat. No. #VCWP04700). Length distribution of the
533 genomic DNA was analyzed by pulsed-field gel electrophoresis, which exhibited an average
534 length of over 2 Mbp. The Chromium library was constructed using the Chromium Genome
535 Reagent Kit v1 Chemistry (10x Genomics, Cat No. #PN-120216), and sequencing was
536 performed with an Illumina HiSeq X to obtain paired-end 151 nt-long reads.
537
538 Genome assembly
539 De novo genome assembly using the Chromium linked-reads was performed with Supernova
540 ver. 2.0.0 (10x Genomics) with the default parameters, and the resultant sequences were output
541 with the option 'pseudohap'. Detection and masking of repetitive sequences were performed
542 using RepeatMasker ver. 4.0.7 (Smit et al, 2013-2015) with NCBI RMBlast ver. 2.6.0+ and the
543 species-specific repeat library from RepBase ver. 23.01.
544
545 Gene model construction
546 Gene models for gene expression level quantification were constructed in the three following
547 steps. First, ab initio gene prediction was performed by BRAKER ver. 2.0.5 (Hoff *et al*, 2019).
548 In this process, GeneMark-ET ver. 4.33 (Lomsadze *et al*, 2014) with the information of spliced
549 RNA-seq alignment was used for training, and AUGUSTUS ver. 3.3 (Stanke *et al*, 2008) with
550 the parameters of `UTR=on, species=human` was used for gene prediction. For the
551 abovementioned training of BRAKER, the RNA-seq reads were aligned to the repeat-masked
552 genome sequences by STAR ver. 2.5.4a (Dobin *et al*, 2013) with default parameters using the
553 entire set of RNA-seq reads of various tissue types (Supplementary Table S7). Second, the
554 information of RNA-seq alignment was directly incorporated into the gene models to improve
555 the coverage of the 3' UTR region of each gene which is not reliably predicted in ab initio gene
556 prediction. This computation was performed with HISAT2 ver. 2.1.0 (Kim *et al*, 2019) and
557 StringTie ver. 1.3.4d (Kovaka *et al*, 2019), whose output GTF file was merged with the gene
558 models produced by BRAKER using the merge function of StringTie. Finally, the existing
559 transcript sequences of MusPutFur1.0 available at NCBI RefSeq (GCF_000215625.1) was
560 incorporated into the gene models by mapping their sequences to the repeat-masked genome
561 sequences using GMAP ver. 2017-11-15 (Wu & Watanabe, 2005) with the `not report chimeric
562 alignments` option. The gene name of each locus was adopted from the annotation in RefSeq,
563 and the gene name of a newly predicted locus was assigned according to the results of a
564 BLASTX search against the UniProtKB Swiss-Prot database release 2020_01. The assignment

565 was performed only for genes with a bit score (in the abovementioned BLASTX search) of
566 greater than 60. When a locus has multiple transcripts, the one with the highest score was
567 adopted for gene naming. If a transcript estimated by ab initio prediction bridged multiple
568 genes, they were incorporated into the gene models as separate genes.
569
570 Completeness assessment of assemblies
571 To assess the continuity of the genome assembly and gene space completeness of the gene
572 models, gVolante ver. 1.2.1 (Nishimura *et al*, 2017) was used with the CEGMA ortholog search
573 pipeline and the reference orthologues gene set CVG (Hara *et al*, 2015).
574
575 ***In utero* and postnatal electroporation**
576 *In utero* electroporation (IUE) and postnatal electroporation in ferrets was performed as
577 described previously (Kawasaki *et al*, 2012; Matsui *et al*, 2013; Tsunekawa *et al*, 2016 for IUE;
578 Borrell, 2010 for postnatal electroporation) with modifications. Briefly, pregnant ferrets or
579 ferret pups were anesthetized with isoflurane at indicated stages of the development. The
580 location of lateral ventricles was visualized with transmitted light delivered through an optical
581 fiber cable. Three µl of plasmid DNA solution was injected into the lateral ventricle at indicated
582 developmental stages using an injector. Each embryo or pup was placed between the paddles
583 of electrodes, and was applied a voltage pulse of 45V at the duration from 100 msec to 900
584 msec (100,0 Pon and 1000,0 Poff) 10 times for in utero electroporation, and under the same
585 condition except a voltage of 60V for postnatal electroporation (CUY21 electroporator, Nepa
586 Gene).
587
588 **Plasmids**
589 To assure a stabilized expression of transgenes, we combined expression vectors with a
590 hyperactive piggyBac transposase system to integrate expression vectors into the genome for
591 a stable expression (Yusa *et al*, 2011). To enrich neural progenitor cell populations in "AG"
592 samples used for the single-cell transcriptome analysis, pLR5-Hes5-d2-AzamiGreen (0.5
593 µg/µl; Hes5 promoter was gifted from Kageyama Laboratory; Ohtsuka *et al*, 2006) was
594 electroporated at E30 for E40, or at E34 for postnatal samples, together with pCAX-hyPBase
595 (0.5 µg/µl). Among them, for P1 and P10 samples, pPB-LR5-mCherry (0.5 µg/µl) was also
596 included in the DNA solution.
597 To sparsely label the cell cytoplasm for detailed imaging of individual cells on vibratome-cut
598 thick cortical sections, we have used pPB-LR5-floxstop-EGFP combined with a low

599 concentration of Cre-expressing plasmid. The concentrations used for these plasmids were 0.5
600 µg/µl or 1.0 µg/µl for a GFP labeling and 1 ng/µl or 10 ng/µl of Cre-expressing plasmid for P0
601 or P5 samples, respectively (Figure 2A). For all electroporation experiments, Fast Green
602 solution (0.1 mg/ml; Wako Pure Chemical Industries) was added into the freshly prepared
603 mixture of plasmid DNA to visualize the injection.
604 For in situ hybridization probes, the PCR product was inserted into pCR-BluntII-TOPO for
605 cloning and sequencing.
606
607 **Library preparation for scRNA-seq**
608 10x v2 Chromium was performed on dissociated single cells according to the manufacturer's
609 protocol.
610
611 **Single cell isolation and sorting of Azamigreen-expressing cells**
612 Cell suspension was prepared as reported previously (Wu *et al*, 2022) with modifications.
613 Brains were collected at indicated stages, transferred in the ice-cold dissection Dulbecco's
614 Modified Eagle Medium (DMEM) F12 and meninges were removed. Somatosensory area was
615 dissected from embryonic or postnatal cortices using an ophthalmic knife (15°) under a
616 dissection microscope. Sliced tissues were dissociated via enzymatic digestion with papain at
617 37°C for 30 - 45 min in ice-cold Hank's Balanced Salt Solution (HBSS) (-) with EDTA (0.1
618 M). Dissociated cells were centrifuged at 1000xg for 5 min to remove papain by washing with
619 PBS and were resuspended in 0.375% BSA/HBSS (-), or in the sorting buffer (DMEM F12 +
620 GlutamaX (Thermo Fisher); 0.1 % of Penicillin/Streptomycin (Millipore); 20 ng/ml human
621 basic FGF, Peprotech; 1xB27 RA-, Gibco) for cell sorting (see below). Homogenous cell
622 suspension filtered through 35 µm strainer (Falcon).
623 To concentrate neural progenitor cell (NPC) populations at the expense of mature neurons, two
624 methods were used for each sample, except for E25, from which cells were collected using
625 whole somatosensory area:
626 1) "T" samples: the cortical plate (CP) of cortical sections were dissected out and a part of the
627 intermediate zone (IZ) was likely to be included in the discarded region.
628 2) "AG" samples: brains collected at indicated stages were electroporated in utero by
629 azamiGreen (AG)-expression vector under the control of Hes5 promoter. The latter method
630 allows the expression of AG in only NPC by the presence of a degradation signal "d2" in the
631 vector to degrade AG protein in HES5-negative differentiating progeny. Only "AG" samples
632 were processed with cell sorting and dissociated cell obtained as described above were placed

633 in a SH800 cell sorter (SONY) to sort azamigreen-positive cells in 0.375%BSA/HBSS(-)
634 solution. Cell survival and cell number were quantified by Countess or Countess II (Invitrogen),
635 prior to an application of single cell isolation using 10x v2 Chromium kit.
636 Samples from the same developmental stage, except for P10 "T" sample, were born from the
637 same mother and were collected by applying either of above methods on the same day and
638 processed in parallel.
639
640 Library preparation and Sequencing
641 Single-cell libraries were generated according to the manufacturer's instructions. Cell
642 suspensions were diluted for an appropriate concentration to obtain 3,000 cells per channel of
643 a 10X microfluidic chip device and were then loaded on the 10X Chromium chips accordingly
644 to the manufacturer's instructions.
645 Total cDNA integrity and quality were assessed with Agilent 2100 Bioanalyzer.
646 Libraries were sequenced on the HiSeq PE Rapid Cluster Kit v2 (Illumina), or the TruSeq PE
647 Cluster Kit v3-cBot-HS, to obtain paired-end 26 nt (Read 1)-98 nt (Read 2) reads.
648
649 **Immunohistology and confocal imaging**
650 Ferret brains were removed from embryos or pups and fixed for 1 or 2 overnights, respectively,
651 in 1% paraformaldehyde (PFA) prepared in 0.1M phosphate buffer (PB, pH 7.4) at 4°C. P35
652 ferrets were transcardially perfused with cold PBS, followed by 4% PFA, under deep
653 anesthesia with isoflurane, then collected brains were post-fixed with 1% PFA. After the
654 fixation of brains or cortical tissue slices after a live imaging, they were equilibrated in 25%
655 sucrose overnight before embedding in O.C.T. compound (TissueTek, Sakura) and frozen in
656 liquid nitrogen. Frozen samples were stored at -80°C prior to a coronal sectioning using a
657 cryostat (CM3050S Leica Microsystems, 12µm sections). After equilibration at room
658 temperature, sections were washed in PBS with 0.1% Tween (PBST), followed by a treatment
659 with an antigen retrieval solution of HistoVT one (Nacalai Tesque) diluted 10 times in milliQ
660 water, at 70°C for 20 min. Sections were then blocked 1 hr at the room temperature (RT) in
661 PBS with 2% Triton-X100 and 2% normal donkey serum (Sigma), followed by an incubation
662 overnight at 4°C with primary antibody diluted in the blocking solution. After washing in PBST
663 three times, sections were treated with appropriate fluorescence-conjugated secondary
664 antibodies (1:500) along with 4',6-diamidino-2-phenylindole (DAPI, 1:1,000) for 1 hr at room
665 temperature. Sections were washed again prior to mounting with PermaFluor solution (Therma
666 Fisher Scientific).

667 Immunostaining of thick ferret brain sections (200 μm) were performed as previously reported
668 (Tsunekawa et al., 2016). Briefly, ferret brains were fixed in 1%PFA, washed in PB overnight
669 at 4°C, and embedded in 4% low-melting agarose (UltraPure LMP agarose, Thermo Fischer
670 Scientific). Embedded brains were sliced coronally at 200 μm thickness by a vibratome
671 (LinerSlicer, DOSAKA EM) on ice. Floating sections were washed three times with PBST,
672 treated with the blocking solution for 1 hour at RT and incubated with primary antibodies for
673 5 or 6 overnights at 4°C under shaking. Sections were then washed in PBST and treated with
674 secondary antibodies for 5 or 6 overnights at 4°C under shaking. After washing, we mounted
675 brain slices with CUBIC solution 2 to allow the transparency.
676 Fluorescent images were acquired using an FV1000 confocal microscope (Olympus, Japan).
677 Somatosensory cortices were captured with 20X or 100X objective lenses. When 100x
678 objective lens was used, z-stacks of confocal images were taken with an optical slice thickness
679 1.0 μm or 1.5 μm and MAX-projection images obtained by FiJi are shown.
680 All the antibodies used in this study are listed in Key Resources Table, and are used at
681 following concentrations: chicken anti-EGFP, 1:500; mouse anti-Alpha B Crystallin, 1:500;
682 Rabbit anti-FoxJ1, 1:500; goat anti-Olig2, 1:500; rat anti-Eomes, 1:500; rabbit anti-Pax6,
683 1:500; mouse anti-Pax6, 1:500; mouse anti Gfap, 1:500; rabbit anti-HopX, 1:500; rat anti-RFP,
684 1:500; goat anti-adenine cyclase III, 1:250; rat anti-Ctip2, 1:500; mouse anti-Satb2, 1:500, rat
685 anti-Ki67, 1:500.
686
687 **Probe preparation**
688 Primers for PCR targeting ferret *CLU* gene were designed with Primer3 ver 0.4.0 software.
689 Total RNA was isolated from embryonic ferret brain, collected in Trizol. cDNA was generated
690 from total RNA using the Prime Script 1st strand cDNA synthesis kit (Takara) according to the
691 manufacturer's recommended procedure. Target cDNA was inserted into pCR-TOPOII-Blunt
692 plasmid for cloning and sequencing using M13F or M13R primers. Anti-sense cRNA probes
693 were then generated by in vitro transcription using T7 promoter.
694
695 ***In situ* hybridization**
696 ISH was performed as described previously, with some modifications (Mashiko *et al*, 2012).
697 Briefly, ferret brains were perfused in 4%PFA in PBS and were fixed at 4%PFA in 0.1M PB,
698 Fixed brain were incubated in 30% sucrose/4%PFA in 0.1M PB for at least 1 day and were
699 stored at -80℃ until ISH. Frozen brains were sectioned in coronal plane at 25 μm using cryostat

700 (CM3050S Leica Microsystems). Sections on slides were post-fixed at 4% PFA in 0.1M PB
701 and treated with proteinase K (Roche). Sections were hybridized with digoxigenin (DIG)-
702 labeled probes at 72° C overnight in hybridization solution. Sections were then washed and
703 blocked with donkey serum and incubated with pre-absorbed DIG antibody, conjugated to
704 Alkaline phosphatase for 2 hours at room temperature. Color development was performed in
705 solution containing NBT/BCIP (Roche).
706
707 **QUANTIFICATION AND STATISTICAL ANALYSIS FOR scRNA-seq.**
708
709 Statistical details including experimental n, statistical tests and significance are reported in
710 Figure Legends.
711
712 **Alignment and raw processing of data**
713 Fastq files were obtained from individual samples and were processed using Cell Ranger
714 pipeline v2. Alignment was done using "Cell Ranger count" function with default parameters
715 accordingly to manufacturer's instructions to map reads to the ferret reference (MPF_Kobe
716 2.0.27). The raw data for each set of cells within a sample was obtained by cellranger count
717 function and was read using Seurat "Read10X" function (Seurat v3.1.5) (Stuart *et al*, 2019),
718 creating a matrix for unique molecular identified (UMI) counts of each gene within each cell.
719
720 **Filtering and normalization**
721 Filtering and normalization were performed using Seurat (v3.1.5) (Stuart *et al*, 2019). Briefly,
722 each sample was filtered by removing low-quality cells with unique feature counts less than
723 200, and genes expressed in less than 3 cells (Seurat function "CreateSeuratObject"). Different
724 samples were then merged using the Seurat "merge" function. Merged data was further subset
725 by keeping cells with features (genes) over 200 and less than 5000. Raw UMI counts were then
726 normalized using "LogNormalize" as normalization method, which divided reads by the total
727 number of UMIs per cell, then multiplied by 10,000 (Seurat "NormalizeData" function). This
728 resulted in a total of 30,234 cells and 19,492 genes: E25 (3486 cells), E34AG (3223 cells),
729 E34T (2260 cells), E40AG (1102), E40T (1581 cells), P1AG (2681), P1T (3641), P5AG (2429),
730 P5T (2926), P10AG (3010) and P10T (3895).
731
732 **Single-cell clustering and visualization**

733 Cell clustering was employed to the entire cell population after removing low-quality cells,
734 using Seurat (v3.1.5) (Stuart *et al*, 2019). 2,000 highly variable genes were identified and used
735 for the downstream analysis using Seurat "FindVariableFeatures" function (selection.method
736 = "vst"), which allowed the calculation of average expression and dispersion for each gene.
737 Normalized data was then processed for scaling using Seurat function "Scale Data" with
738 default settings, which also allowed the regression of the batch. Principal component analysis
739 (PCA) was performed with 2,000 variable genes to reduce dimensionality of the scaled dataset
740 and 50 PCs were retained (Seurat "RunPCA" function). Clustering was then performed using
741 graph-based clustering approach ("Find Neighbors" function) using top 20 PCs, which were
742 selected based on the standard deviation of PCs on the elbowplot created by Seurat function
743 "ElbowPlot" and based on statistical significance calculated by JackStraw application. Briefly,
744 cells are embedded in a k-nearest neighbor (KNN) graph based on the Euclidean distance in a
745 PCA space. Then, this knn graph is used to group cells on a shared nearest neighbor graph
746 based on calculations of overlap between cells with similar gene expression patterns (Jaccard
747 similarity). Cells were then clustered by Louvain algorithm implemented in Seurat
748 "ClusterCells" function (resolution = 0.8, dims = 1:20). Next, we used Seurat "RunUMAP"
749 function, which resulted in cell clusters being separated in embedding space while preserving
750 the balance between local and global structure.
751
752 **Cluster annotations**
753 Cluster markers were obtained using "FindAllMarkers" Seurat function. We tested genes that
754 showed at least a 0.25-fold difference between the cells in the cluster and all remaining cells,
755 and that were detected in more than 25% of the cells in the cluster. Clusters, which we called
756 subtypes, were then annotated by comparing cluster markers to previously identified cell type
757 markers in the literature for mouse and human datasets. The full list of markers is given under
758 Table S1. The heatmap in **Fig. 2B** shows the expression data for the top 10 highly expressed
759 marker genes for each cluster using a downsampling of maximum 500 cells from each cluster.
760 Plotting cells onto the UMAP plot by their batch indicated that batches did not influence
761 clustering (**Fig. S2A**) in accordance with the differential expression of cluster markers (**Fig.
762 2B, S3A)**. When a cluster was enriched based on the developmental stage, the information was
763 included in the annotation. For example, "early RG" cluster was enriched in E25 samples, and
764 expressed both common radial glial cell markers shared with other RG clusters in our dataset,
765 but also expressed early onset-genes reported in mouse studies (Okamoto *et al*, 2016; Telley *et*

766 *al*, 2019), such as *HMGA2*, *FLRT3*, *LRRN1* (Table S1). Therefore, we named this cluster as
767 "early RG" based on its age-dependent properties.
768 To achieve more precise clustering, cycling cells were identified with known markers
769 implemented in Seurat package (S genes and G2M genes). Clusters enriched in S genes or
770 G2M genes were identified, including early_RG2 (S), early_RG3 (G2M), late_RG2 (G2M),
771 late_RG3 (S), IPC2 (S) and IPC3 (G2M) (**Fig. S3C**). Subtypes of RG and IPC clusters were
772 further combined to facilitate the data representation (**Fig. 2B**).
773
774 **Differential gene expression analysis**
775 Differential gene expression (DEG) analysis was assessed using "FindMarkers" Seurat
776 function with default parameters.
777
778 **Pseudotime analysis**
779 Monocle 2 was used to construct developmental trajectories based on pseudotime ordering of
780 single cells (Qiu *et al*, 2017; Trapnell *et al*, 2014). We generated a subset of clusters using
781 "SubsetData" Seurat function using the raw counts. Combined progenitor clusters (F_earlyRG,
782 F_midRG, F_lateRG, F_tRG, F_IPC, F_OPC) were selected. All clusters known to be
783 generated from a non-cortical origin including microglia, endothelial and mural cells, were
784 removed prior the pseudotime analysis. The expression matrix and a metadata file that
785 contained above cluster information defined by Seurat were used as input for monocle package
786 (**Table S2**).
787 The "differentialGeneTest" function was used to select genes for dimensionality reduction
788 (fullModelFormulaStr = '~Subtype.combined'). Top 1,000 genes were then applied for cell
789 ordering. The visualization of the minimum spanning tree on cells was obtained by Monocle2
790 "plot_complex_cell_trajectory" function. To visualize the ordered cells on Seurat's UMAP
791 plot, we extracted the branch information for cells and added as metadata of the merged Seurat
792 object ("AddMetaData" Seurat function).
793
794 **Processing External scRNA-seq Datasets for comparisons and preprocessing**
795 scRNA-seq data of developing human brain from Nowakowski *et al*. (2017), from Bhaduri *et*
796 *al*. (2021) were used for cross-species comparisons (**Figures 6, 7, S7-S9**). All cells included in
797 the analysis and cluster assignments from the provided matrix were mapped to the cell type
798 assignments provided in the metadata of Nowakowski et al. dataset and the cell type labels
799 were used as provided by the authors without modification. For Bhaduri et al. dataset, GW25

sample was used for clustering by Seurat package as described above. For both, we removed low quality cells and clusters annotated based on anatomical regions other than somatosensory cortex, and removed cells with less than 200 features. For Bhaduri et al. dataset, we filtered to cells with at least 200 features, less than 6,500 features and less than 5% mitochondrial genes. This resulted in 25,485 cells from around 180,000 cells in Bhaduri et al. dataset, and in 2,673 cells in Nowakowski et al. dataset.

For organoid datasets, Herring et al. (2022) and Bhaduri et al., (2021) were used (**Figs. S8, S9**) with default settings in Seurat. The data driven from organoids at 5-months, 9-months, 12-months and organoids at 3-weeks, 5-weeks, 8-weeks, 10-weeks were used for Herring and Bhaduri datasets, respectively.

Integrated analysis of human and ferret scRNA-seq datasets

Human datasets published by Bhaduri *et al*. (2021) and Nowakowski *et al*. (2017) were used for integration analysis with our ferret dataset using Seurat canonical correlation analysis (Stuart *et al*, 2019). First, a Seurat object was created for all datasets as described previously. Briefly, each object was individually processed with a normalization and variable features were identified. For human datasets, we excluded cells or samples obtained from anatomical regions other than somatosensory cortex. Then, the integration anchors between human and ferret Seurat objects were identified using "FindIntegrationAnchors" Seurat function with default settings. The integration was then performed with "IntegrateData" Seurat function. Scaling, PCA and UMAP dimensional reduction were performed to visualize the integration results.

Cluster correlation analysis between ferret and human clusters.

Correlation analysis was performed as described by Bhaduri *et al*. (2020), with modifications. Briefly, lists of cluster marker genes obtained by "FindAllMarkers" Seurat function on individual datasets were extracted prior to an integration (Table S5A), except for Nowakowski et al dataset, for which the marker gene list was provided. A score based on the specificity and the enrichment of cluster marker genes was generated (defined as "Genescore"). A genescore value was obtained by the multiplication of the average fold change that represents the gene enrichment, with the percentage of the cells expressing the marker in the cluster (pct.1) divided the percentage of the cells from other clusters expressing the marker (pct.2: specificity). This function was employed on the marker genes for a human subtype of interest in the space of marker genes for ferret NPC (RG, IPC, OPC and EP) clusters. Genescores for both ferret and human were then obtained for all markers shared between human subtype of interest (i.e. oRG)

834 and ferret NPC subtypes. We then applied cor.test function using Pearson method to estimate
835 a correlation and the significance of the correlation for the obtained genescores between ferret
836 and human samples. These resulting values were represented for NPC subtypes on heatmap
837 plots.
838
839 **Prediction of oRG-like/tRG-like cells by cross-dataset analysis.**
840 The cell type marker genes for oRG and tRG cell types were extracted from each human
841 scRNAseq datasets. To predict human oRG-like and tRG-like cells in ferret sample more
842 precisely, we removed mature neuron, microglia, and endothelia clusters, as well as clusters
843 assigned as unknown, from individual datasets for an integration between ferret and human
844 NPC clusters using Seurat package as described in the above section (Stuart *et al*, 2019). After
845 identification of anchors between human and ferret Seurat objects using
846 "FindIntegrationAnchors", we extracted the information of each pair of anchors, which
847 including one ferret and one human cell. If the human cell in the pair belongs to oRG (tRG)
848 cluster in human dataset, we consider the other ferret cell in the same pair as oRG (tRG)-like
849 cell.
850
851 **Cluster score calculation.**
852 Based on a genescore calculated for marker genes as previously described, a cell-type
853 predictive model was generated. For both datasets, our custom-made R scripts were applied to
854 generate matrices using either human oRG markers or tRG markers using our integrated
855 subsets. In the space of matrices reduced with corresponding human marker genes, a score we
856 defined as "oRG score" or "tRG score" was created by multiplying human genescore for each
857 marker genes with the expression values of these genes in all cells present in the integrated
858 subset data. The results were represented by beeswarm and boxplot.
859
860 **Evaluation of immunolabeled cell number and statistical analysis**
861 The counting frames on images of immunolabeled sections consisted of 150 μm of width
862 regions of interests (ROIs). The numbers of immunolabeled cells within selected ROIs were
863 manually counted using the "cell counter" tool of FiJi software (Schindelin *et al*, 2012). The
864 VZ was identified by its cell density visualized by DAPI, and according to its thickness
865 measured by a vertical length from the ventricular surface at indicated stages (100 μm at P5,
866 70 μm at P10). The proportions of immunolabeled cells positive for various markers were

867 calculated using the summed data counted within all ROIs. The data obtained from lateral
868 cortices of somatosensory area was averaged from 2 to 3 sections.
869 For CRYAB-positive cells, we only counted cells with nuclei which were visualized by DAPI
870 staining. The numbers of positive cells were counted using two or three different animals.
871 Quantification was followed by Wilcoxon test to assess statistical significance and data on each
872 section were considered as n = 1.
873
874 **Quantification of RNAscope in situ hybridization and immunostaining image**
875 Images of RNAscope in situ hybridization and FOXJ1 immunostaining were captured by using
876 an IX83 inverted microscope (Olympus) equipped with Dragonfly 200 confocal unit (Andor),
877 Zyla Z4.2 sCMOS camera (Andor), and UPLXAPO 60XO objective lens (Olympus). Imaging
878 was performed to satisfy Nyquist sampling (xy = 48 nm/pixel by using 2x zoom optic and z =
879 136 nm interval) and 3D deconvolution was performed by ClearView-GPU™ option of Fusion
880 software (Andor). Default deconvolution parameter is used except for number of irritation (n
881 = 24) and mounting media reflection index (RI = 1.46). For quantification of images,
882 CellProfiler version 4.2.4 (Stirling *et al*, 2021) was used. To detect mRNA dots of RNAscope
883 in situ hybridization images, a single Z section of deconvolved images were processed by
884 EnhancingSpeckles module (10 pixels size) and then mRNA dots were detected by
885 IdentifyPrimaryObjects module, adaptive Otsu two class method, using default parameter
886 except for size of adaptive window (size = 10). Dot's diameter less than 4 pixels were removed
887 as a background noise. Cytoplasmic ROIs were generated from smoothed RNAscope in situ
888 hybridization images by MedianFilter module (window size = 10) and manually drawn seed
889 ROIs of DAPI staining images by using IdentifySecondaryObjects module (propagation
890 adaptive Otsu two class method, using default parameter). FoxJ1 immunostaining raw images
891 were measured by MeasureImageIntensity module. Quantified data were visualized and
892 clustered by using RStudio (version 2022.07.1+554) with R (version 4.0.3). Each of mRNA
893 count data and protein staining intensity data was log transformed and normalized, and
894 hierarchical clustering was done by using a Euclidian distance and complete clustering method
895 and cut tree to 4 clusters. Each cluster expression was plotted and classified to single or double
896 positive, or double negative of SPARCL1 and FOXJ1 populations.
897
898 **Data and code availability**
899 Genome assembly and chromium linked-read sequences were deposited in the DDBJ under
900 accession numbers BLXN01000001–BLXN01022349 and DRA010274. The gene models are

available from Figshare under the DOI: 10.6084/m9.figshare.12807032. Single-cell RNA-seq data have been deposited in the DDBJ under the DRR Run accession number DRR496478-DRR496488. Codes used for analysis can be found in https://github.com/wuquan723/Ferret-single-cell-data-from-Matsuzaki-lab. Any information required to obtain and reanalyze the data reported in this paper is available from the lead contact upon request.

Acknowledgements

We thank Kazuaki Yamaguchi, Rohab F. Abdelhamid, and Chiharu Tanegashima for sequencing RNA and genomic DNA and all members of the Laboratory of Cell Asymmetry for providing technical support and helpful discussions. We also thank an anonymous reviewer 1 of Review Commons for his/her constructive suggestions, and Fumiya Kusumoto for his continuous encouragement. This work was supported by JSPS KAKENHI [Grant Numbers 18H04003, 17H05779, 19H04791] and RIKEN. RIKEN funds F.M. M.B. was a RIKEN International Program Associate. Q.W. was supported by a JSPS Postdoctoral Fellowship and a RIKEN Special Postdoctoral Researcher Program.

Author contributions

M.B., Q.W., and F.M. designed experiments. M.K., O.N., Q.W., Y.K., and S.K. constructed new ferret gene models. M.B. and Q.W. performed scRNA-seq experiments and bioinformatics analyses. M.B., Y.T., and Q.W. performed molecular biological analyses. M.B., T.S. [Taeko] and T.S. [Tomomi] performed histological analyses. A.S and Q.W. performed and analyzed RNA/protein double-tissue staining. T.S. [Taeko] carried out time-lapse imaging. T.S. [Taeko], Y.T. and H.K. bred the ferrets. M.B., Q.W., A.S. and F.M. wrote the manuscript. All authors read and approved the final manuscript for submission.

Competing interests statement

The authors declare no competing interests.

References

Bhaduri A, Andrews MG, Mancia Leon W, Jung D, Shin D, Allen D, Jung D, Schmunk G, Haeussler M, Salma J, *et al* (2020) Cell stress in cortical organoids impairs molecular subtype specification. *Nature* 578(7793): 142–148

Bhaduri A, Sandoval-Espinosa C, Otero-Garcia M, Oh I, Yin R, Eze UC, Nowakowski TJ &

936 Kriegstein AR (2021) An atlas of cortical arealization identifies dynamic molecular
937 signatures. *Nature* 598(7879): 200–204
938 Borrell V (2010) In vivo gene delivery to the postnatal ferret cerebral cortex by DNA
939 electroporation. *J Neurosci Methods* 186: 186–195
940 Capecchi MR & Pozner A (2015) ASPM regulates symmetric stem cell division by tuning
941 Cyclin E ubiquitination. *Nat Commun* 6:8763
942 Chapman B & Stryker MP (1992) Origin of orientation tuning in the visual cortex. *Curr Opin*
943 *Neurobiol* 2: 498–501
944 Chenn A & McConnell SK (1995) Cleavage orientation and the asymmetric inheritance of
945 Notch1 immunoreactivity in mammalian neurogenesis. *Cell* 82: 631–641
946 DeAzevedo LC, Fallet C, Moura-Neto V, Daumas-Duport C, Hedin-Pereira C & Lent R
947 (2003) Cortical radial glial cells in human fetuses: Depth-correlated transformation into
948 astrocytes. *J Neurobiol* 55(3): 288–298
949 Dobin A, Davis CA, Schlesinger F, Drenkow J, Zaleski C, Jha S, Batut P, Chaisson M &
950 Gingeras TR (2013) STAR: ultrafast universal RNA-seq aligner. *Bioinformatics* 29: 15–
951 21
952 Eiraku M, Watanabe K, Matsuo-Takasaki M, Kawada M, Yonemura S, Matsumura M,
953 Wataya T, Nishiyama A, Muguruma K & Sasai Y (2008) Self-organized formation of
954 polarized cortical tissues from ESCs and its active manipulation by extrinsic signals.
955 *Cell Stem Cell* 3: 519–532
956 Fietz SA, Kelava I, Vogt J, Wilsch-Bräuninger M, Stenzel D, Fish JL, Corbeil D, Riehn A,
957 Distler W, Nitsch R, *et al* (2010) OSVZ progenitors of human and ferret neocortex are
958 epithelial-like and expand by integrin signaling. *Nat Neurosci* 13(6): 690–699
959 Fujimori A, Itoh K, Goto S, Hirakawa H, Wang B, Kokubo T, Kito S, Tsukamoto S &
960 Fushiki S (2014) Disruption of Aspm causes microcephaly with abnormal neuronal
961 differentiation. *Brain Dev* 36(8): 661–669
962 Gertz CC & Kriegstein AR (2015) Neuronal Migration Dynamics in the Developing Ferret
963 Cortex. *J Neurosci* 35: 14307–14315
964 Hansen D V., Lui JH, Parker PRL & Kriegstein AR (2010) Neurogenic radial glia in the
965 outer subventricular zone of human neocortex. *Nature* 464(7288): 554–561
966 Hara Y, Tatsumi K, Yoshida M, Kajikawa E, Kiyonari H & Kuraku S (2015) Optimizing and
967 benchmarking de novo transcriptome sequencing: From library preparation to assembly
968 evaluation. *BMC Genomics* 16: 1–12
969 Herring CA, Simmons RK, Freytag S, Poppe D, Moffet JJD, Pflueger J, Buckberry S,
970 Vargas-Landin DB, Clément O, Echeverría EG, *et al* (2022) Human prefrontal cortex
971 gene regulatory dynamics from gestation to adulthood at single-cell resolution. *Cell* 185:
972 4428-4447.e28
973 Hoff KJ, Lomsadze A, Borodovsky M & Stanke M (2019) Whole-Genome Annotation with
974 BRAKER. *Methods Mol Biol* 1962: 65–95
975 Huang W, Bhaduri A, Velmeshev D, Wang S, Wang L, Rottkamp CA, Alvarez-Buylla A,
976 Rowitch DH & Kriegstein AR (2020) Origins and Proliferative States of Human
977 Oligodendrocyte Precursor Cells. *Cell* 182(3): 594-608.e11
978 Jackson CA, Peduzzi d. J & Hickey TL (1989) Visual cortex development in the ferret. I.
979 Genesis and migration of visual cortical neurons. *J Neurosci* 9: 1242–1253
980 Jayaraman D, Kodani A, Gonzalez DM, Mancias JD, Mochida GH, Vagnoni C, Johnson J,
981 Krogan N, Harper JW, Reiter JF, *et al* (2016) Microcephaly Proteins Wdr62 and Aspm
982 Define a Mother Centriole Complex Regulating Centriole Biogenesis, Apical Complex,
983 and Cell Fate. *Neuron* 92(4): 813–828
984 Johnson MB, Sun X, Kodani A, Borges-Monroy R, Girskis KM, Ryu SC, Wang PP, Patel K,
985 Gonzalez DiM, Woo YM, *et al* (2018) Aspm knockout ferret reveals an evolutionary

986 mechanism governing cerebral cortical size. *Nat 2018 5567701* 556: 370–375
987 Johnson MB, Wang PP, Atabay KD, Murphy EA, Doan RN, Hecht JL & Walsh CA (2015)
988 Single-cell analysis reveals transcriptional heterogeneity of neural progenitors in human
989 cortex. *Nat Neurosci* 18(5): 637–646
990 de Juan Romero C, Bruder C, Tomasello U, Sanz-Anquela JM & Borrell V (2015) Discrete
991 domains of gene expression in germinal layers distinguish the development of
992 gyrencephaly. *EMBO J* 34(14): 1859–1874
993 Kawasaki H, Iwai L & Tanno K (2012) Rapid and efficient genetic manipulation of
994 gyrencephalic carnivores using in utero electroporation. *Mol Brain* 5:24
995 Kawaue T, Shitamukai A, Nagasaka A, Tsunekawa Y, Shinoda T, Saito K, Terada R, Bilgic
996 M, Miyata T, Matsuzaki F, *et al* (2019) Lzts1 controls both neuronal delamination and
997 outer radial glial-like cell generation during mammalian cerebral development. *Nat*
998 *Commun* 10(1):2780
999 Kessaris N, Fogarty M, Iannarelli P, Grist M, Wegner M & Richardson WD (2006)
1000 Competing waves of oligodendrocytes in the forebrain and postnatal elimination of an
1001 embryonic lineage. *Nat Neurosci 2005 92* 9: 173–179
1002 Kim D, Paggi JM, Park C, Bennett C & Salzberg SL (2019) Graph-based genome alignment
1003 and genotyping with HISAT2 and HISAT-genotype. *Nat Biotechnol 2019 378* 37: 907–
1004 915
1005 Kou Z, Wu Q, Kou X, Yin C, Wang H, Zuo Z, Zhuo Y, Chen A, Gao S & Wang X (2015)
1006 CRISPR/Cas9-mediated genome engineering of the ferret. *Cell Res* 25(12): 1372–1375
1007 Kovaka S, Zimin A V., Pertea GM, Razaghi R, Salzberg SL & Pertea M (2019)
1008 Transcriptome assembly from long-read RNA-seq alignments with StringTie2. *Genome*
1009 *Biol* 20: 1–13
1010 Liu J, Liu W, Yang L, Wu Q, Zhang H, Fang A, Li L, Xu X, Sun L, Zhang J, *et al* (2017) The
1011 Primate-Specific Gene TMEM14B Marks Outer Radial Glia Cells and Promotes
1012 Cortical Expansion and Folding. *Cell Stem Cell* 21(5): 635-649.e8
1013 Liu J, Wu X & Lu Q (2022) Molecular divergence of mammalian astrocyte progenitor cells
1014 at early gliogenesis. *Development* 149(5): de
1015 Lomsadze A, Burns PD & Borodovsky M (2014) Integration of mapped RNA-Seq reads into
1016 automatic training of eukaryotic gene finding algorithm. *Nucleic Acids Res* 42
1017 Mashiko H, Yoshida AC, Kikuchi SS, Niimi K, Takahashi E, Aruga J, Okano H & Shimogori
1018 T (2012) Comparative Anatomy of Marmoset and Mouse Cortex from Genomic
1019 Expression. *J Neurosci* 32: 5039–5053
1020 Matsui A, May T, C. YA, S. KS, Mami U, Masaharu O & Tomomi S (2013) BTBD3
1021 Controls Dendrite Orientation Toward Active Axons in Mammalian Neocortex. *Science*
1022 *(80-)* 342(6162): 1114–1118
1023 McConnell SK (1988) Fates of visual cortical neurons in the ferret after isochronic and
1024 heterochronic transplantation. *J Neurosci* 8: 945–974
1025 McConnell SK (1995) Constructing the cerebral cortex: Neurogenesis and fate determination.
1026 *Neuron* 15: 761–768
1027 McInnes L, Healy J & Melville J (2018) UMAP: Uniform Manifold Approximation and
1028 Projection for Dimension Reduction. *arXiv* doi: 1802.
1029 Nishimura O, Hara Y & Kuraku S (2017) gVolante for standardizing completeness
1030 assessment of genome and transcriptome assemblies. *Bioinformatics* 33: 3635–3637
1031 Noctor SC, Scholnicoff NJ & Juliano SL (1997) Histogenesis of Ferret Somatosensory
1032 Cortex. *J Comp Neurol* 387: 179–193
1033 Nowakowski TJ, Bhaduri A, Pollen AA, Alvarado B, Mostajo-Radji MA, Di Lullo E,
1034 Haeussler M, Sandoval-Espinosa C, Liu SJ, Velmeshev D, *et al* (2017) Spatiotemporal
1035 gene expression trajectories reveal developmental hierarchies of the human cortex.

1036 *Science (80-)* 358(6368): 1318–1323
1037 Nowakowski TJ, Pollen AA, Sandoval-Espinosa C & Kriegstein AR (2016) Transformation
1038 of the Radial Glia Scaffold Demarcates Two Stages of Human Cerebral Cortex
1039 Development. *Neuron* 91(6): 1219–1227
1040 Ohtsuka T, Imayoshi I, Shimojo H, Nishi E, Kageyama R & McConnell SK (2006)
1041 Visualization of embryonic neural stem cells using Hes promoters in transgenic mice.
1042 *Mol Cell Neurosci* 31(1): 109–122
1043 Okamoto M, Miyata T, Konno D, Ueda HR, Kasukawa T, Hashimoto M, Matsuzaki F &
1044 Kawaguchi A (2016) Cell-cycle-independent transitions in temporal identity of
1045 mammalian neural progenitor cells. *Nat Commun* 7:11349
1046 Ortiz-Álvarez G, Daclin M, Shihavuddin A, Lansade P, Fortoul A, Faucourt M, Clavreul S,
1047 Lalioti ME, Taraviras S, Hippenmeyer S, *et al* (2019) Adult Neural Stem Cells and
1048 Multiciliated Ependymal Cells Share a Common Lineage Regulated by the Geminin
1049 Family Members. *Neuron* 102(1): 159-172.e7
1050 Polioudakis D, de la Torre-Ubieta L, Langerman J, Elkins AG, Shi X, Stein JL, Vuong CK,
1051 Nichterwitz S, Gevorgian M, Opland CK, *et al* (2019) A Single-Cell Transcriptomic
1052 Atlas of Human Neocortical Development during Mid-gestation. *Neuron* 103(5): 785-
1053 801.e8
1054 Pollen AA, Nowakowski TJ, Chen J, Retallack H, Sandoval-Espinosa C, Nicholas CR, Shuga
1055 J, Liu SJ, Oldham MC, Diaz A, *et al* (2015) Molecular Identity of Human Outer Radial
1056 Glia during Cortical Development. *Cell* 163(1): 55–67
1057 Pulvers JN, Bryk J, Fish JL, Wilsch-Bräuninger M, Arai Y, Schreier D, Naumann R, Helppi
1058 J, Habermann B, Vogt J, *et al* (2010) Mutations in mouse Aspm (abnormal spindle-like
1059 microcephaly associated) cause not only microcephaly but also major defects in the
1060 germline. *Proc Natl Acad Sci U S A* 107(38): 16595–16600
1061 Qiu X, Mao Q, Tang Y, Wang L, Chawla R, Pliner HA & Trapnell C (2017) Reversed graph
1062 embedding resolves complex single-cell trajectories. *Nat Methods* 14: 979–982
1063 Rash BG, Duque A, Morozov YM, Arellano JI, Micali N & Rakic P (2019a) Gliogenesis in
1064 the outer subventricular zone promotes enlargement and gyrification of the primate
1065 cerebrum. *Proc Natl Acad Sci* 116(14): 7089 LP – 7094
1066 Rash BG, Duque A, Morozov YM, Arellano JI, Micali N & Rakic P (2019b) Gliogenesis in
1067 the outer subventricular zone promotes enlargement and gyrification of the primate
1068 cerebrum. *Proc Natl Acad Sci* 116(14)
1069 Reillo I & Borrell V (2012) Germinal Zones in the Developing Cerebral Cortex of Ferret:
1070 Ontogeny, Cell Cycle Kinetics, and Diversity of Progenitors. *Cereb Cortex* 22: 2039–
1071 2054
1072 Reillo I, De Juan Romero C, García-Cabezas MÁ & Borrell V (2011) A role for intermediate
1073 radial glia in the tangential expansion of the mammalian cerebral cortex. *Cereb Cortex*
1074 21: 1674–1694
1075 Rowitch DH & Kriegstein AR (2010) Developmental genetics of vertebrate glial–cell
1076 specification. *Nature* 468(7321): 214–222
1077 Saadoun S & Papadopoulos MC (2010) Aquaporin-4 in brain and spinal cord oedema.
1078 *Neuroscience* 168(4): 1036–1046
1079 Schindelin J, Arganda-Carreras I, Frise E, Kaynig V, Longair M, Pietzsch T, Preibisch S,
1080 Rueden C, Saalfeld S, Schmid B, *et al* (2012) Fiji: an open-source platform for
1081 biological-image analysis. *Nat Methods 2012 97* 9: 676–682
1082 Shitamukai A, Konno D & Matsuzaki F (2011) Oblique radial glial divisions in the
1083 developing mouse neocortex induce self-renewing progenitors outside the germinal zone
1084 that resemble primate outer subventricular zone progenitors. *J Neurosci* 31: 3683–3695
1085 Sidman RL & Rakic P (1973) Neuronal migration, with special reference to developing

1086 human brain: a review. *Brain Res* 62(1): 1–35
1087 Smart IHM, Dehay C, Giroud P, Berland M & Kennedy H (2002) Unique Morphological
1088 Features of the Proliferative Zones and Postmitotic Compartments of the Neural
1089 Epithelium Giving Rise to Striate and Extrastriate Cortex in the Monkey. *Cereb Cortex*
1090 12(1): 37–53
1091 Stanke M, Diekhans M, Baertsch R & Haussler D (2008) Using native and syntenically
1092 mapped cDNA alignments to improve de novo gene finding. *Bioinformatics* 24: 637–
1093 644
1094 Stirling DR, Swain-Bowden MJ, Lucas AM, Carpenter AE, Cimini BA & Goodman A
1095 (2021) CellProfiler 4: improvements in speed, utility and usability. *BMC Bioinformatics*
1096 22
1097 Stuart T, Butler A, Hoffman P, Hafemeister C, Papalexi E, Mauck WM, Hao Y, Stoeckius M,
1098 Smibert P & Satija R (2019) Comprehensive Integration of Single-Cell Data. *Cell*
1099 177(7): 1888-1902.e21
1100 Tanegashima C, Nishimura O, Motone F, Tatsumi K, Kadota M & Kuraku S (2018)
1101 Embryonic transcriptome sequencing of the ocellate spot skate Okamejei kenojei. *Sci*
1102 *Data 2018 51* 5: 1–6
1103 Telley L, Agirman G, Prados J, Amberg N, Fièvre S, Oberst P, Bartolini G, Vitali I, Cadilhac
1104 C, Hippenmeyer S, *et al* (2019) Temporal patterning of apical progenitors and their
1105 daughter neurons in the developing neocortex. *Science* 364
1106 Trapnell C, Cacchiarelli D, Grimsby J, Pokharel P, Li S, Morse M, Lennon NJ, Livak KJ,
1107 Mikkelsen TS & Rinn JL (2014) The dynamics and regulators of cell fate decisions are
1108 revealed by pseudotemporal ordering of single cells. *Nat Biotechnol* 32(4): 381–386
1109 Tsunekawa Y, Terhune RK, Fujita I, Shitamukai A, Suetsugu T & Matsuzaki F (2016)
1110 Developing a de novo targeted knock-in method based on in utero electroporation into
1111 the mammalian brain. *Development* 143(17): 3216–3222
1112 Wu Q, Shichino Y, Abe T, Suetsugu T, Omori A, Kiyonari H, Iwasaki S & Matsuzaki F
1113 (2022) Selective translation of epigenetic modifiers affects the temporal pattern and
1114 differentiation of neural stem cells. *Nat Commun 2022 131* 13: 1–18
1115 Wu TD & Watanabe CK (2005) GMAP: a genomic mapping and alignment program for
1116 mRNA and EST sequences. *Bioinformatics* 21: 1859–1875
1117 Yamamoto S, Yamashita A, Arakaki N, Nemoto H & Yamazaki T (2014) Prevention of
1118 aberrant protein aggregation by anchoring the molecular chaperone αB-crystallin to the
1119 endoplasmic reticulum. *Biochem Biophys Res Commun* 455: 241–245
1120 Yu X, Ng CP, Habacher H & Roy S (2008) Foxj1 transcription factors are master regulators
1121 of the motile ciliogenic program. *Nat Genet* 40(12): 1445–1453
1122 Yusa K, Zhou L, Li MA, Bradley A & Craig NL (2011) A hyperactive piggyBac transposase
1123 for mammalian applications. *Proc Natl Acad Sci U S A* 108: 1531–1536
1124 Zheng K, Wang C, Yang J, Huang H, Zhao X, Zhang Z & Qiu M (2018) Molecular and
1125 Genetic Evidence for the PDGFRα-Independent Population of Oligodendrocyte
1126 Progenitor Cells in the Developing Mouse Brain. *J Neurosci* 38: 9505–9513
1127 Zhong S, Zhang S, Fan X, Wu Q, Yan L, Dong J, Zhang H, Li L, Sun L, Pan N, *et al* (2018)
1128 A single-cell RNA-seq survey of the developmental landscape of the human prefrontal
1129 cortex. *Nature* 555(7697): 524–528
1130 Smit, AFA, Hubley, R & Green, P. (2013-2015) *RepeatMasker Open-4.0*. Available at:
1131 http://www.repeatmasker.org.

1132 **FIGURE LEGENDS**

1133 **Figure 1- Improvement of the gene model for scRNA-seq of ferretes.**

1134 **A** Schematic representing cortical development and emergence of diverse neural progenitors
1135 in humans and ferrets. Progenitors sequentially generate DL- and subsequent UL-neurons, and
1136 finally glial cells, and form ependymal cells. RG and oRG have been morphologically and
1137 positionally identified in both humans and ferrets while tRG have been only reported in humans.
1138 VZ, ventricular zone; ISVZ, inner subventricular zone; OSVZ, outer subventricular zone; IZ,
1139 intermediate zone; DL, deep layer; UL, upper layer; CP, cortical plate; NEP cell,
1140 neuroepithelial cell; Mn, migrating neuron; and EP cell, ependymal cell.

1141 **B** Schematic representing the experimental design and time points used to build the
1142 transcriptome atlas of developing somatosensory cortex of ferrets. Single cells were isolated
1143 using 10X Chromium (see **Materials and Methods**).

1144 **C** Linkage of the 3'UTR sequence and the coding sequence of genes has been improved in this
1145 study. This linkage is necessary to assign the gene coding for a mRNA as far as 10x Genomics
1146 Chromium kit is used for scRNA-seq (see **Materials and Methods**).

1147 **D** Table comparing quality-control metrics of an alignment with either MusPutFur 1.0 (UCSC
1148 gene models) or MusPutFur 2.60 (this study) using E34 samples. The total number of genes
1149 detected and median genes per cell were higher with MusPutFur 2.60.

1150 **E** Violin plots showing the number of genes, mRNAs and the percentage of mitochondrial
1151 genes per cell in each sample and time point.

1152

1153 **Figure 2 - Single-cell RNA-seq reveals ferret transcriptome signatures and the cell types.**

1154 **A** UMAP visualization showing cells colored by Seurat clusters and annotated by cell types
1155 (as shown in **C, D**).

1156 **B** Heatmap showing expression profiles of cluster marker genes based on log fold-change
1157 values. Cells were grouped by Seurat clustering (transverse). Cell types were assigned
1158 according to the expression of marker and differentially expressed genes in each cluster. Early
1159 RG was defined by the expression of *HMGA2, LDHA,* and *LIX1*; and late RG, by *PTN, ALDOC,*
1160 and *FABP7*. OPC, oligodendrocyte precursor cell; ITN, interneuron; and EN, endothelial cells.
1161 Other cell type abbreviations are shown in **Fig. 1A** and the main text. Color bar matches the
1162 Seurat clusters in (**A**). The ten most enriched representative genes in each cluster are shown,
1163 with typical marker genes noted in (**C**–**E**).

1164 **C** Normalized expression levels of representative marker genes of different cell types projected
1165 onto the UMAP plot in (**A**). MG, microglia.

1166 **D** Expression pattern of *CRYAB*, a marker for tRG, only described in humans and other
1167 primates.
1168 **E** The expression pattern of *HOPX*, a marker for oRG in humans and other primates in the
1169 UMAP plot.
1170
1171 **Figure 3 - Truncated tRG emerges during postnatal cortical development in ferrets.**
1172 **A** Representative images showing the cellular features of tRG and aRG in VZ at P0, and P5,
1173 respectively, stained for GFP (red) and CRYAB (green). RG cells were sparsely labelled with
1174 a GFP-expressing plasmid at E30 via IUE for P0 samples, and at P3 for P5 samples. MAX
1175 projection was performed on a 30 μm vibratome section with 5 μm or 2.5 μm interval for each
1176 z-image at P0 or P5, respectively. Scale bar, 50 μm.
1177 **B** Expression patterns of CRYAB (green) and PAX6 (red) in ferret germinal zones during
1178 postnatal development (P1, P5, and P10) (cryosection thickness = 12 μm).
1179 **C** Developmental profile of CRYAB expression in ferret cortices. Immunostaining for CRYAB
1180 (green) and DAPI (gray) on cryosections at E32, E38, P3, P5, and P10 (cryosection thickness
1181 = 12 μm).
1182 **D** Quantification of $CRYAB^+$ cells among all nuclei (DAPI) in VZ strips through
1183 immunostaining, indicating a great increase in CRYAB-expressing cells (strip width = 150 μm;
1184 n = 3 for P5; n = 2 for P10; Wilcoxon rank-sum test *p*-value = 6.574e-08).
1185 **E–G** Expression of other markers in $CRYAB^+$ cells. Representative images taken with a 100X-
1186 objective are shown with MAX projection. The border of VZ is shown with a white line. Below
1187 each double staining image, quantification of KI67-, TBR2-, or OLIG2-expressing cells among
1188 the $CRYAB^+$ cell population in the VZ is shown (n = 2 for P5; n = 2 for P10 for each staining
1189 except n = 3 for TBR2 staining). Box and whisker plots indicate ranges (lines) and upper and
1190 lower quartiles (box) with the median. Scale bars, 20 μm.
1191
1192
1193 **Figure 4 - Temporal fates of RG cells predicted by pseudo-time trajectory analysis.**
1194 **A** Pseudo-time trajectory tree of progenitor cells in the ferret developing cortex (assembled
1195 with Monocle v2). Cellular distribution at each state is the same as in the UMAP plot shown
1196 in Fig. 1C. Cell types representing each state and their gene markers are shown next to each
1197 state (see below).
1198 **B** Trajectory trees split by collection stages (AG samples are shown).

1199 **C** Distribution of cells expressing marker genes for stem cell states (*HES1* and *HMGA2*) and
1200 the neurogenic state (*EOMES*) along trajectories. Color densities indicate the log-normalized
1201 unique molecular identifier count for each gene.
1202 **D** Normalized expression of three genes: *SPARCL1, CRYAB,* and *FOXJ1* in the state 6 and
1203 state 7 cells in the pseudotime trajectory tree (**A**). The combination of expression levels of the
1204 four markers gene discriminates state 6 (ependymal) and state 7 (astrogenic). See the text for
1205 details.
1206 **E** Distribution of tRG cells along the tree and tRG-focused UMAP visualization. The tRG cells
1207 (n = 162) were found on the three states, NPC3 (9.3%; 15 cells), ependymal-tRG (61.1%; 99
1208 cells), and astrogenic-tRG (29.6%; 48 cells).
1209 **F** Composition of the three types of tRG in (D) by the collection stage (AG and T samples are
1210 combined). No tRG cells were collected from E25 and E34.
1211
1212 **Figure 5 - tRG adopt both ependymal cells and astrogenic fates in ferrets.**
1213 **A** Immunostaining of 12 µm cortical cryosections with CRYAB (green) and FOXJ1 (red),
1214 focusing on the VZ at E40, P3, P5, P10, P14, and P35. Scale bar, 50 µm. CRYAB and FOXJ1
1215 double positive nuclear rows are shown with arrowheads at P5 and P10 when this nuclear
1216 alignment is visible.
1217 **B** Percentage of FOXJ1 expression in CRYAB-expressing cells (n = 3 for P5; n = 2 for P10;
1218 Wilcoxon rank sum test *p*-value = 1.749e-05). Images with merged channels in A are shown
1219 with the same color codes, antibodies and scale bars as A.
1220 **C** Number of cells expressing both *CRYAB* and *FOXJ1* in the mid and late RG, or tRG clusters
1221 shown in Fig. 1C (with unique molecular identifier counts higher than 0.25). Colored bars
1222 indicate the stages of sample collection. *CRYAB*- and *FOXJ1*-expressing cells increased over
1223 time only in the tRG cluster.
1224 **D** Normalized expression levels of *FOXJ1* in each cell in the indicated ferret clusters in Fig.
1225 1C.
1226 **E** Cortical origin and shape of FOXJ1-expressing ependymal cells indicated with white arrows.
1227 Staining for FOXJ1 at P14 after labeling cortical progenitors with an mCherry-expressing
1228 vector via IUE at E30. The maximum projection images with 1 µm z-step size are shown.
1229 Cryosection thickness = 12 µm; scale bar = 20 µm.
1230 **F** Normalized expression of *SPARCL1* and *FOXJ1* in each cell in ferret tRG clusters separated
1231 by the pseudo-time trajectory analysis (see **Table S3**).

1232 **G** Relationship between *SPARCL1* and *FOXJ1* transcripts in individual cells within each tRG
1233 cluster. Within the 15 cells that were classified in state 5 tRG, only one expressed *FOXJ1*
1234 mRNA. Pearson relationship analysis was performed using cells from state 6 and 7 (R=0.19 p
1235 value=0.018).
1236 **H** Immunostaining of a P10 cortical tissue for FOXJ1 protein and S*PARCL1* mRNA.
1237 **I** Cells within the VZ in (**H**) were clustered into four classes by FOXJ1 protein± and S*PARCL1*
1238 mRNA±. Cluster A: S*PARCL1*/FOXJ1-/-, B: S*PARCL1*/FOXJ1 +/-, C: S*PARCL1*/FOXJ1-/+,
1239 D: S*PARCL1*/ FOXJ1 +/+ (Fig. S5C, S5D, Table S4). See **Materials and Methods** for
1240 clustering. Scale bar = 20 μm.
1241
1242 **Figure 6 – Comparison of molecular identity of RG subtypes between ferret and human.**
1243 **A** UMAP visualization of integrated human (n = 2,672; left) and ferret (n=30,234; right) single-
1244 cell datasets colored according to the different clusters. The names of clusters from human and
1245 ferret cells begin with "H" and "F," respectively.
1246 **B** Homologous temporal pattern of transcriptomic characters of progenitors and their progenies
1247 between ferrets and humans. Corresponding neurogenic stages between ferrets and humans can
1248 be assigned by cell distribution at homologous positions in UMAP plots. Gliogenic RG cells
1249 (a subtype of the "late_RG" group and OPC in **Fig. 2A**) were first distinguished
1250 transcriptionally at ferret E40 and at human GW14, as pointed out by arrows.
1251 **C, D** Correlation coefficient (**C**) and significance (**D**) between indicated clusters of ferrets and
1252 humans, calculated by marker gene scores. See **the text** and **Materials and Methods** for
1253 details.
1254 **E** Normalized expression levels of the indicated genes in humans and ferrets from each
1255 progenitor cluster. See **the text** and **Materials and Methods** for details.
1256 **F** tRG scores of the indicated clusters are presented as box and whisker plots for humans and
1257 ferrets. As for the definition of cluster scores, see **the text** and **Material and Methods**. These
1258 represent the range without outliers (lines) and upper and lower quartiles with the median (box).
1259 Outliers are represented as points outside the box. Outliers are 1.5-fold larger or smaller than
1260 interquartile range from the third or first quartile, respectively.
1261
1262 **Figure 7 - Identification of tRG subtypes in humans and oRG in ferrets.**

A UMAP visualization of human brain cells at GW25 (and removing neurons and other cell types). Cells are colored by cell type and identified by marker genes (data from Bhaduri et al, 2021).

B Schematic of the integration strategy of human and ferret subtypes. We merged the two datasets by pairing mutual nearest neighbor cells (MNN) following canonical correlation analysis (CCA) across species (Stuart and Butler et al, 2019).

C UMAP visualization of integrated ferret and human datasets colored and numbered by different clusters.

D, E Identification of three tRG subtypes in ferrets (D) and humans (E). The red dots highlight the indicated tRG subtypes named after pseudotime trajectory analysis in **Fig. 4**: presumptively "uncommitted", "astrogenic" and "ependymal".

F Distribution of humans (left) and ferrets (right) tRG in the integrated dataset. Human and ferret tRG were identified from the separated dataset. The numbering corresponds to cluster numbers in the integrated clustering (**C**) of human and ferret datasets.

G Distribution of ferret tRG subtypes (identified by the pseudo-time analysis) in the integrated dataset. A major cell population of each of the 3 ferret tRG subtypes (classified by the pseudo-time analysis), more or less, belongs to a single cluster in ferret-human integrated clustering; astrogenic tRG corresponds to cluster 21; ependymal tRG to cluster 20; uncommitted tRG to cluster 7.

H Identification of oRG-like cells in ferret (left) and oRG cells in human (right), by the same way that we have done for tRG. All cells highlighted as red dots.

I oRG scores for oRG-like cells and other NPCs in ferrets. The result indicates that oRG-like cells share more transcriptomic features than other NPCs, whereas ordinary clustering among ferret NPCs failed to distinguish oRG-like cells from the rest. Box and whisker plots indicate ranges (lines) and upper and lower quartiles with the median (box).

J The expression levels of *CRYM*, *CLU*, and *HOPX* in oRG-like cells and other NPCs in ferrets.

1292 **Supplementary Figure Legends**

1293

1294 **Figure S1 - Temporal pattern of neurogenesis and gliogenesis in the cerebral cortex of**
1295 **ferrets.**

1296 **A** Coronal section of the dorsal cortices immunostained for RG (PAX6, red), IPC (TBR2,
1297 green), and OPC (OLIG2, cyan) from early to late neurogenesis at E25, E32, E36, E40, P5,
1298 and P10. Scale bars = 100 μm. The position of the image strip at each stage is shown in the
1299 corresponding dorsal hemisphere image above the strip. The approximative boundaries of
1300 dorsal cortex area used for single-cell RNA sequencing are highlighted with dotty line
1301 segments in the dorsal cortex hemisphere above each strip.

1302 **B** Immunostaining for CTIP2 (green) and SATB2 (red) at the same developmental stages as in
1303 (**A**), showing the onset of DL- (E25 or earlier) and UL-neurogenesis (E32–E34). Scale bars =
1304 100 μm.

1305 **C** Immunostaining for GFAP, a marker showing gliogenic potential, in cortical germinal layers
1306 at E32, E36, E40, P5, and P10. Gliogenic progenitors emerge around E40, while mature
1307 astrocytes with a typical astrocytic morphology appear later at approximately P10 onward in
1308 the outside of the germinal layers (Reillo & Borrell, 2012).

1309 **D, E** mCherry labeling of the dorsal cortex at E30 showing that a population of OLIG2^{+}
1310 oligodendrocyte precursors are generated in the cerebral cortex by P10.

1311 **E.** As reported for both mice and humans (Zheng *et al*, 2018; Rash *et al*, 2019b; Huang *et al*,
1312 2020; Kessaris *et al*, 2006). Arrowheads in the cropped images of the left panels (E area in Fig.
1313 S1**D**) indicate cells that co-express mCherry, PAX6, and OLIG2 in the OSVZ. Scale bars = 20
1314 μm.

1315

1316 **Figure S2 – Quality and reproducibility of ferret single cell transcriptome dataset.**

1317 **A** The brain region used for the cellular isolation for a scRNA-seq are shown. Dotty lines
1318 indicate the approximative boundaries where the cortical slices were cut.

1319 **B** Separate UMAP plots for each cell collection series that was prepared by different
1320 methods, after merged clustering. Left is the "AG" sample: FACS-based sorting of the neural
1321 stem cell fraction labeled with an AzamiGreen (AG)-driven by *HES5* promoter (Ohtsuka et
1322 al, 2006). The "T" samples are shown in the right: cells forming the VZ, SVZ, and
1323 intermediate zones (IZ) of cerebral cortices after discarding the cortical plate. E25 cells,
1324 which were mostly RG, were not collected by cell sorting and put between AG and T in
1325 UMAP plots.

1326 **C** Effects of cell filtration according to the mitochondrial content. We set the threshold to
1327 10%, resulting in 28,686 cells in our dataset, and then performed the workflow from the
1328 normalization step with the same settings that had been applied to our original ferret dataset
1329 (Methods). Left is clusters after the 10% -filtered subset on UMAP, and the original clusters
1330 in **Fig. 2A** is right. Both conditions gave 26 clusters, and both major cell types and subtypes
1331 were conserved after filtering.

1332 **Figure S3 - Cell types in developing ferret cerebral cortex.**

1333 **A**. Dotplot showing average expression and percentage of expression of representative marker
1334 genes for individual cell types in the merged dataset. The largest cluster was composed of UL
1335 neurons, and their four clusters (**Fig. 2A**) were combined as a single "UL" group. P.E.,
1336 percentage of expressing cells per cell type; A.E., average expression per cell type.

1337 **B**. Percentage of sample collection stages in each cell type (top half) and percentage of each
1338 cell type in the merged dataset (bottom half).

1339 **C.** Heatmap showing the expression level of cell cycle marker genes based on log fold-change
1340 values. *PCNA*, *DUT*, *SIVA1,* and *TYMS* are markers of the S-phase; *UBE2C*, *CDCA4*, *CENPF,*
1341 and *CCNB1* are markers of the G2M-phase. Three subclusters among early RG, late RG, and
1342 IPC clusters expressed different markers for cell-cycle states. The color bar at the top indicates
1343 Seurat clusters matching those in **Fig. 2A**.

1344 **D.** Immunostaining for CRYAB$^+$ tRG (green) and HOPX$^+$ RG (red) together with DAPI on P1
1345 and P10 germinal layers.

1346

1347 **Figure S4 - Development of ferret tRG during postnatal cortical development.**

1348 **A** Pie charts showing the percentage of *CRYAB* expression in the ferret clusters of the merged
1349 transcriptome dataset of all stages (**Fig. 2**). Cells were counted as positive if unique molecular
1350 identifier counts for *CRYAB* were > 1 using Seurat "WhichCells" function (slot = "counts").

1351 **B** Number of cells in the tRG clustered by age annotated in the ferret transcriptome dataset
1352 (**Fig. 2**).

1353 **C.** Number of *CRYAB*-expressing cells in RG clusters of the transcriptome dataset (**Fig. 2**).
1354 *CRYAB* expression was undetectable at E25. *CRYAB*-expressing cells in the midRG and lateRG
1355 subtypes did not change in all stages (cell numbers: 58, 46, 68, 55, and 61 at E34, E40, P1, P5,
1356 and P10, respectively), while the number of *CRYAB*$^+$ tRG cells increased after birth (cell
1357 numbers: 0, 21, 50, 91, and 118 at E34, E40, P1, P5, and P10, respectively).

1358 **D–F.** Violin plots indicating the normalized expression of *CRYAB* (**D**), *TBR2* or *EOMES* (**E**),
1359 and *OLIG2* (**F**) in the ferret clusters shown in **Fig. 2**.
1360 **G.** Cellular features of a tRG cell in cortex labelled with GFP at embryonic stages via IUE.
1361 Vibratome sections at P0 and P4 (thickness = 200 μm) were immunostained
1362 **Figure S5 - Temporal fates of RG cells identified by pseudo-time trajectory analysis**
1363 **A.** Ferret cells used for pseudo-time trajectory analysis were lined up along the stretched
1364 pseudo-time axis. Expression levels of markers for typical cell types are also shown along the
1365 pseudo-time axis: *LIX1* and *HMGA2* for early RG, *EOMES* and *NEUROG2* for IP, *RGS20*, and
1366 *PTN* for late RG, *PDGFR* and *OLIG2* for glial cells, and *FOXJ1* and *FAM216B* for ependymal
1367 cells.
1368 **B.** Branching trees labelled by pseudo-time score. Color scale indicates log10 (pseudo-time
1369 +0.1) values. Each state is named after the major cell type.
1370 **C.** The composition of each state is shown by clusters defined in the UMAP plot (**Fig. 2A**).
1371 Percentages for clusters were calculated from all cells in each state.
1372 **D.** Branching trees split by UMAP clusters (**Fig. 2**).
1373
1374 **Figure S6 - Ferret tRG adopt both ependymal and astrogenic fates in ferrets**
1375 **A.** Onset of ciliogenesis in the developing cortex of ferrets, shown via staining for ADENINE
1376 CYCLASE III (cyan) along the VZ surface at E40, P5, P10, and P35. Scale bars = 10 μm.
1377 **B.** Normalized expression of *SPARCL1*/cell in the major cell types shown in **Fig. 2A**.
1378 **C.** Plots showing *SPARCL1* mRNA count (left) and normalized FOXJ1 protein levels (right)
1379 in each cell clustered into individual classes (**A–D**) within the VZ shown in Fig. 4**H** (Table S4).
1380 The box and whisker plots indicate the range (lines) and the upper and lower quartiles with the
1381 median (box).
1382 **D.** Distances of each cell (its center of gravity) from the apical surface in the individual clusters
1383 (**A–D**), as indicated by the box and whisker plots in (**C**). Cluster C and D cells are significantly
1384 located on the apical surface compared to cluster B cells. Data normality was analyzed by
1385 Anderson-Darling test and statical significance was calculated by Kruskal-Wallis test with
1386 Dunn's multiple comparisons test.
1387
1388
1389 **Figure S7 - Comparison of molecular identity of RG subtypes between ferret and human**

1390 **A.** UMAP visualization of integrated ferret (n = 30,234) and human (n = 2,672) single-cell
1391 datasets colored according to the different clusters. The names of clusters from human and
1392 ferret cells begin with "H" and "F," respectively.
1393 **B.** Expression patterns of the indicated genes in each cluster. Circle color indicates the
1394 expression level of each gene. Circles size indicates the percentage of cells expressing the gene
1395 in the indicated cluster.
1396
1397 **Figure S8 - Comparison of the tRG and oRG subtypes between ferrets and humans**
1398 **A, B** Matrices of correlations between two arbitrary RG subtypes from humans and ferrets by
1399 calculating marker gene scores as described for Fig. 5. (**A**) Correlations and (**B**) *p*-values
1400 between pairs in human and ferret clusters are shown. The early RG in ferrets showed the
1401 highest similarity with "OLIG1" in human data. This might be because of two reasons; (1) cells
1402 only at GW25 without early RG were used for comparison, and (2) cells in "OLIG1" highly
1403 expressed genes related with cell proliferation, as the early RG also did (**Table S6**). We did not
1404 observe any cell types in human data corresponding to the ferret "mid RG" with the same
1405 reason described above.
1406 **C** Distribution of human and ferret tRGs in the integrated dataset. The number in the X-axis
1407 indicates the cluster number identified by the UMAP in **Fig. 7C**.
1408 **D** Expression levels of the subtype maker genes in the three tRG-enriched clusters (7, 21, and
1409 28). Marker enrichment is consistent with the presumptive identification of tRG subtypes
1410 according to pseudotime trajectory analysis.
1411 **E** Expression patterns of *CRYM*, *CLU*, and *HOPX* in oRG cells and other NPCs in humans.
1412 **F** *In situ* hybridization of *CLU* at the ferret cortex showed its expression in all VZ, ISVZ, and
1413 OSVZ at P5.
1414
1415 **Figure S9– The absence of a tRG cluster in human organoid datasets.**
1416 **A.** UMAP visualization of human organoid-driven cells colored by the original annotations for
1417 the cell line (left), age (middle) or state (right). Human organoid dataset from Bhaduri et al.,
1418 2020 was used. Bhaduri dataset contained organoids generated from 4 different lines, which
1419 showed a variability in terms of cell distribution on UMAP while overall temporal and
1420 differentiation axes were recapitulated.
1421 **B.** UMAP visualization of cells by clusters (left), original cluster annotations (middle), or by
1422 the normalized expression level of *CRYAB* (right). Red circles on UMAP highlight the group
1423 of cells expressing *CRYAB*. *CRYAB* expression was restricted to two out of four cell lines.

1424 CRYAB was expressed in clusters 26 and 30 enriched in the YH10 line, and cluster 29 enriched
1425 in the13234 cell line.
1426 **C.** UMAP visualization of integrated primary and organoid datasets from Bhaduri et al., 2020.
1427 Cells are colored by the originated dataset (left), primary tRG cluster (middle) or organoid
1428 dataset (right). Black circles were used to indicate the overlap of the region where human
1429 primary tRG was found. Human tRG did not overlap with organoid cells. We found that
1430 CRYAB-expressing organoid clusters 26 and 30 overlapped with "oRG/astrocyte" clusters of
1431 primary tissues.
1432 **D.** UMAP visualization of cells derived from Herring et al., 2022 human organoid dataset,
1433 colored by clusters (left) or by the normalized expression level of *CRYAB* (right).

Figure.1. Improvement of the gene model for scRNA-seq of ferrets.

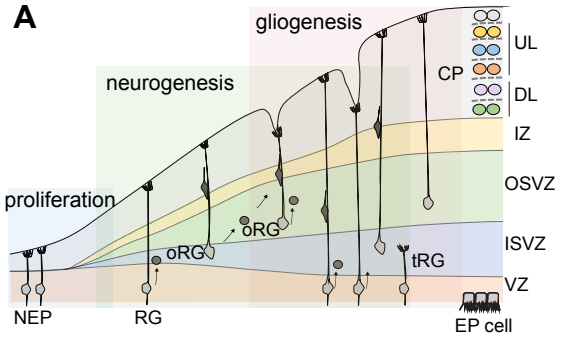

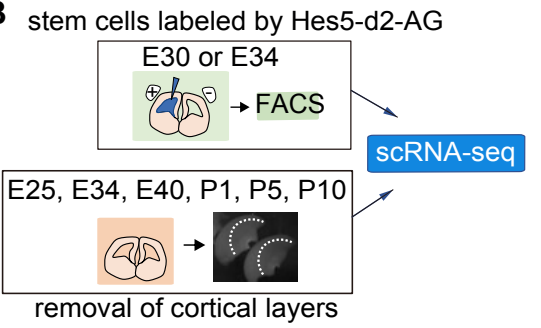

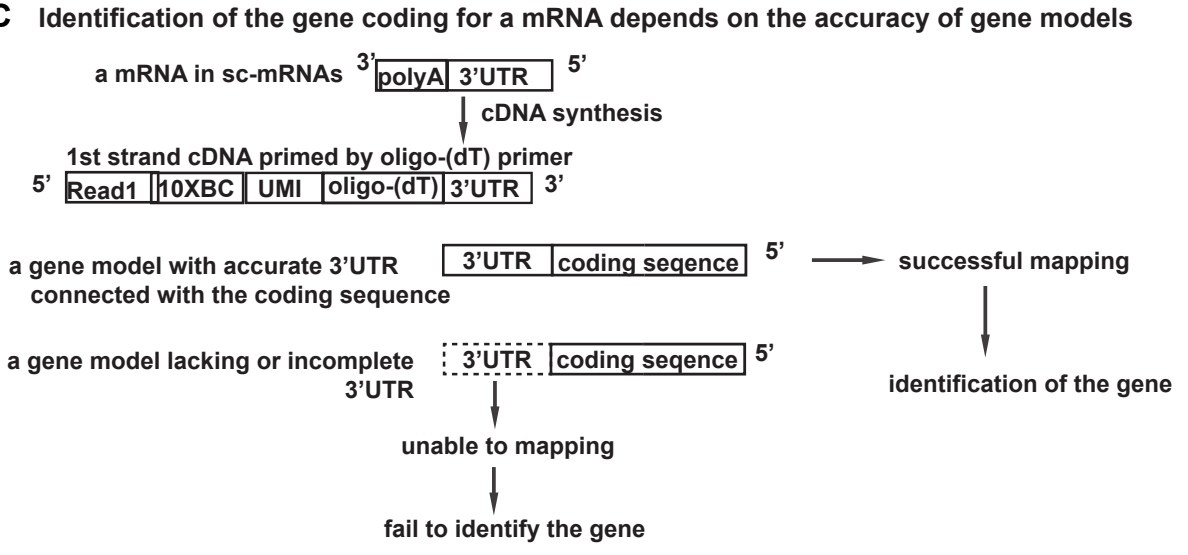

D

	Reference		Median Genes per Cell	Number of Reads	Reads Mapped to Transcriptome	Total Genes Detected	Median UMI Counts
E34_AG	NCBI	3,226	953	137,673,935	30.70%	14,562	2,153
E34_AG	This study	3,223	1,763	137,673,935	58.20%	17,886	3,983
E34_T	NCBI	2,260	1,182	107,508,876	29.90%	14,445	3,096
E34_T	This study	2,265	2,195	107,508,876	56.40%	17,838	5,863

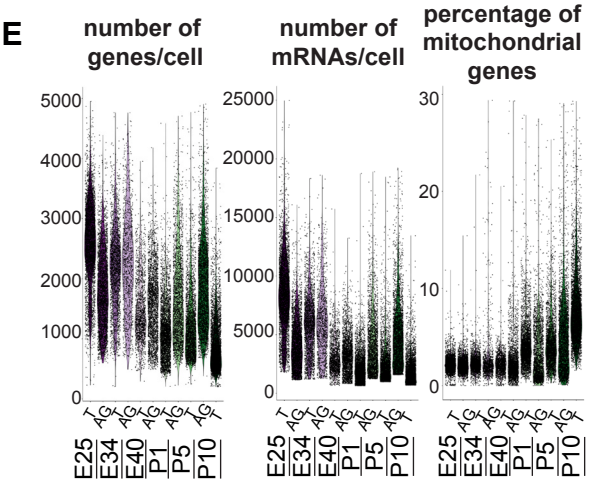

Figure 2. Cell types in developing ferret cerebral cortex.

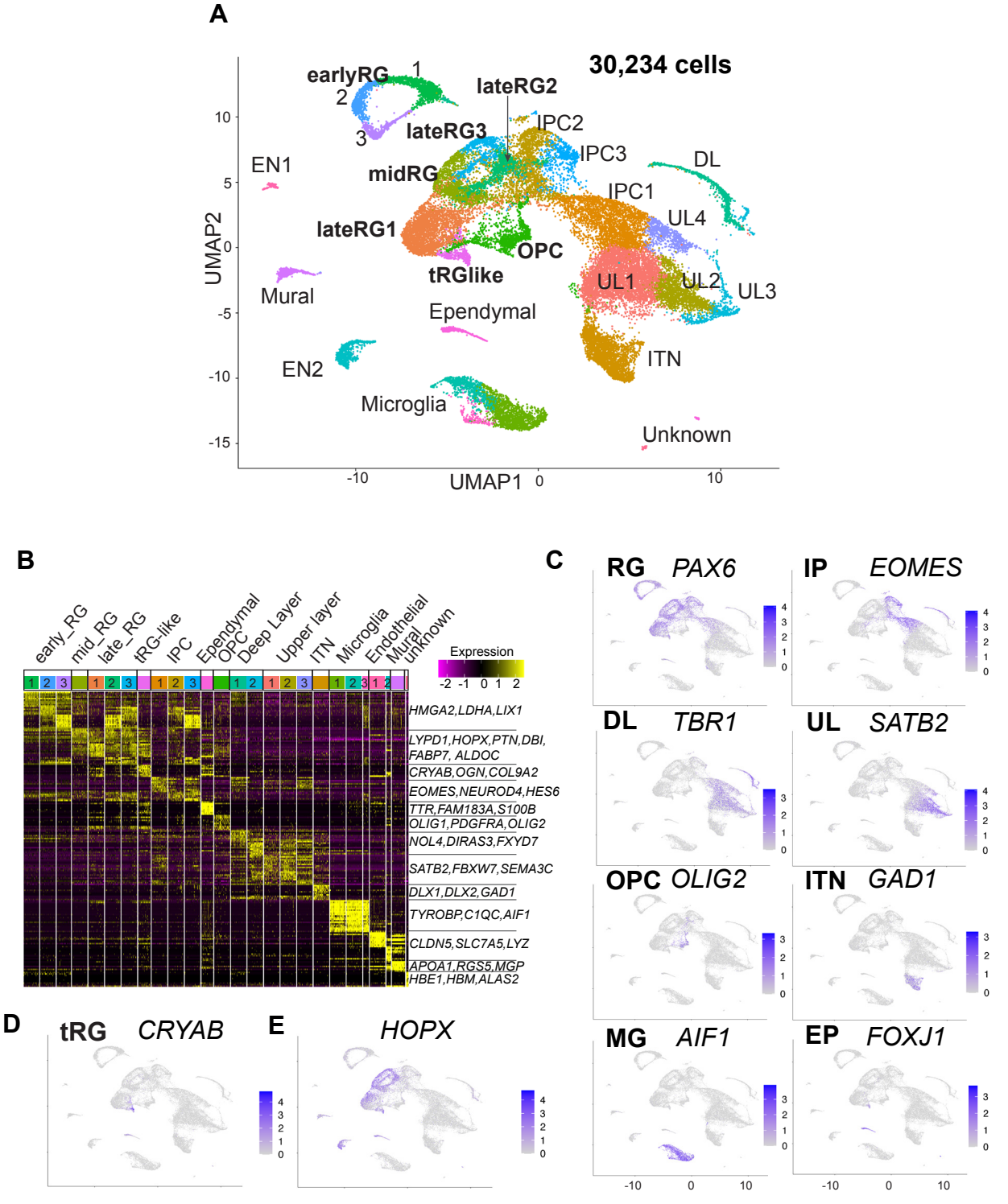

Figure 3. Emergence of ferret tRG during post-natal cortical development.

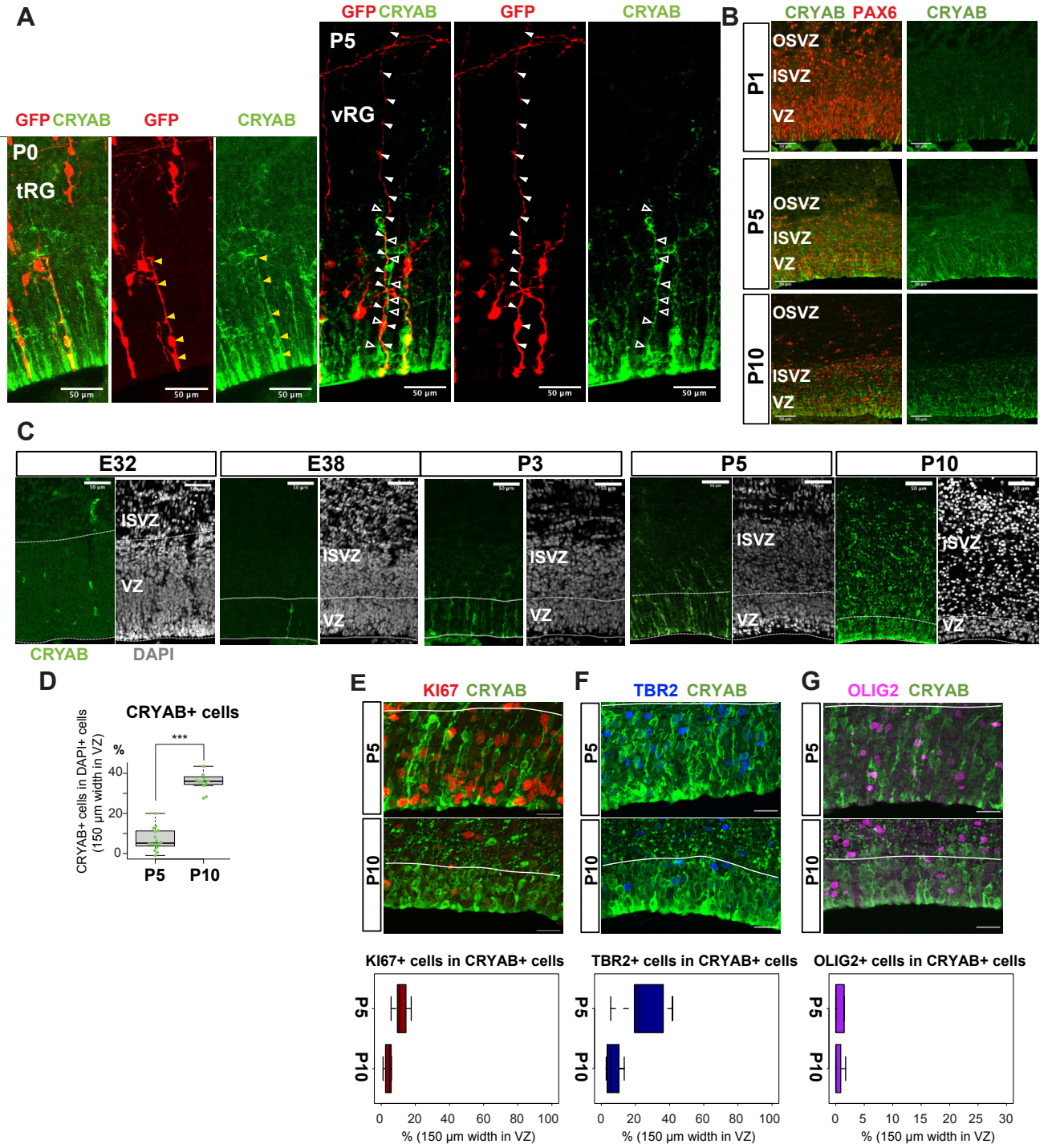

Figure 4. Temporal fates of RG cells predicted by pseudo-time trajectory analysis.

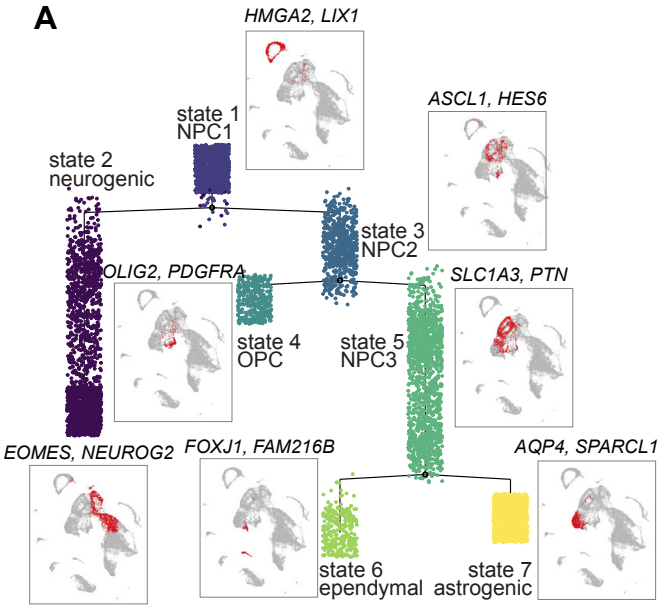

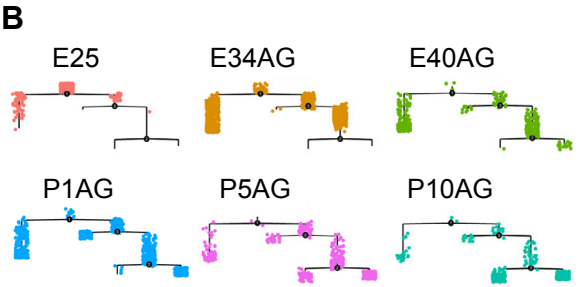

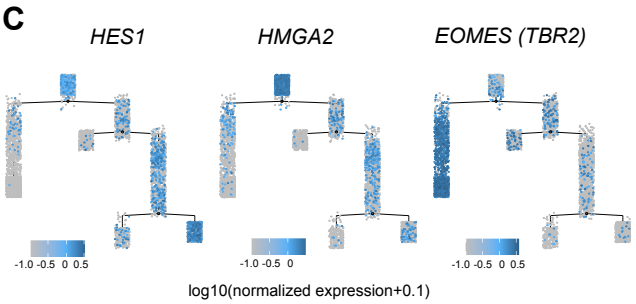

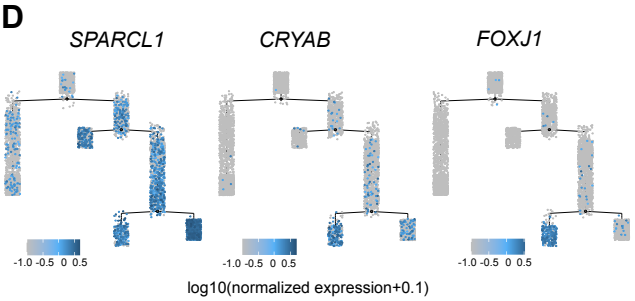

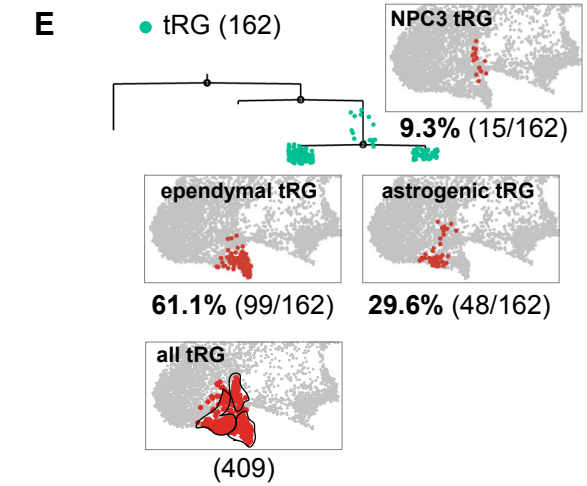

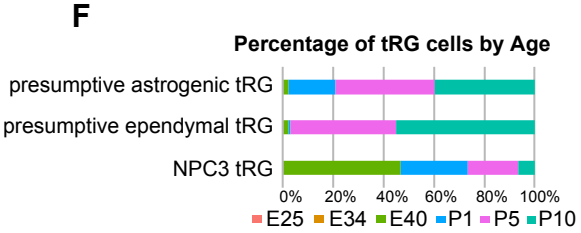

Figure 5. tRG adopt both ependymal and astrogenic fates in ferrets.

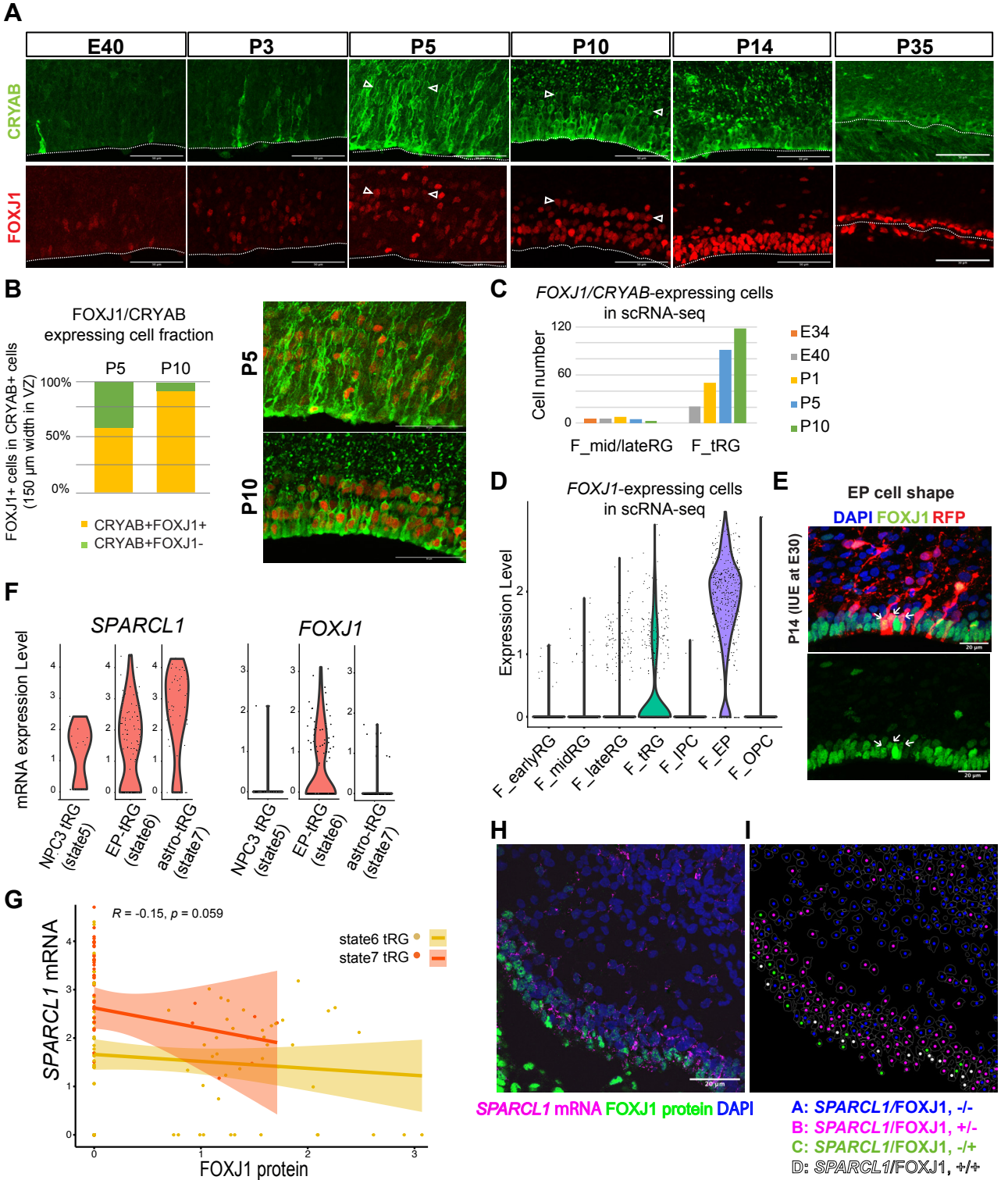

Figure 6. Comparison of molecular identity of RG subtypes between ferret and human.

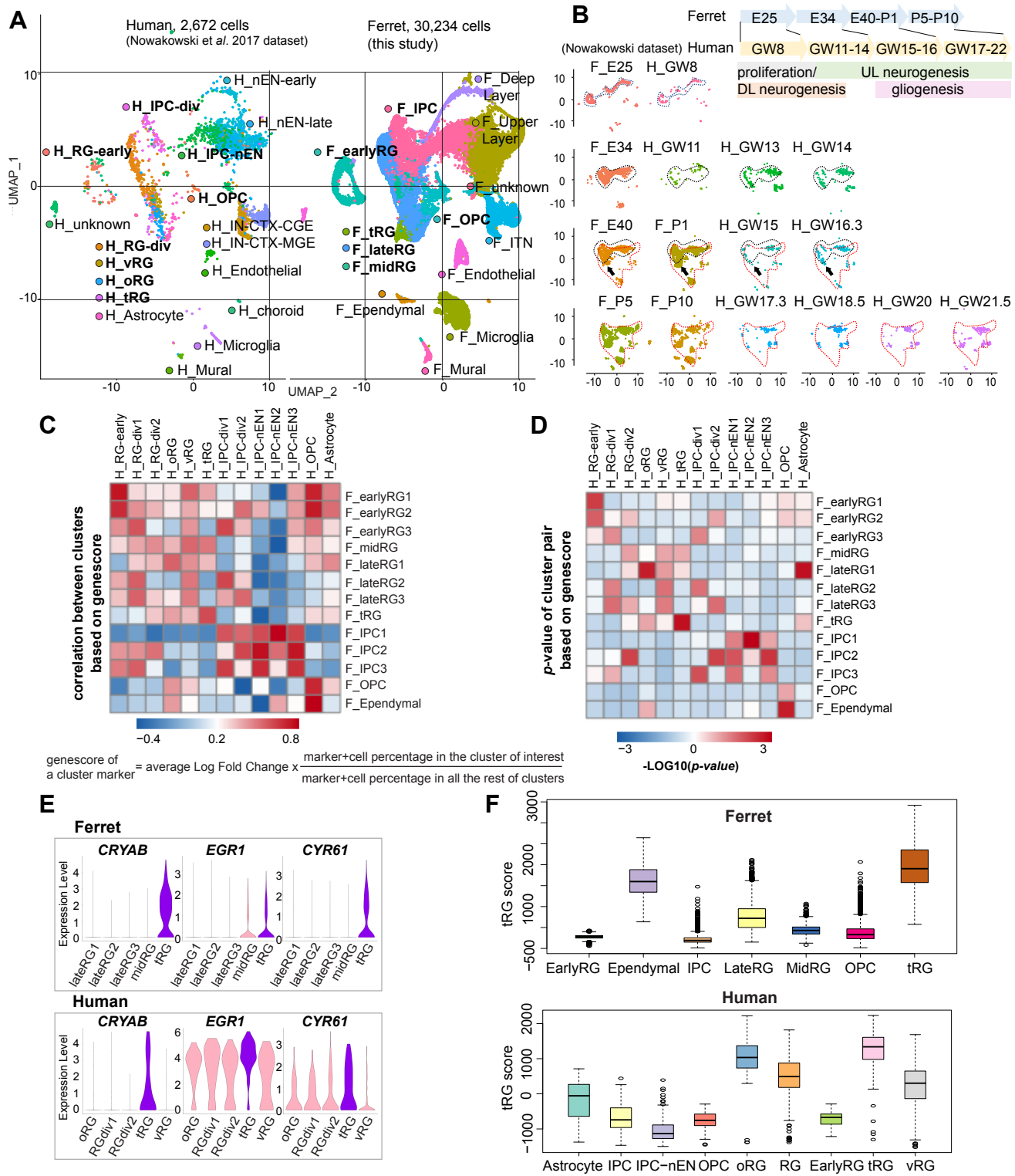

Figure 7. Comparison of the tRG and oRG subtypes between ferrets and humans.

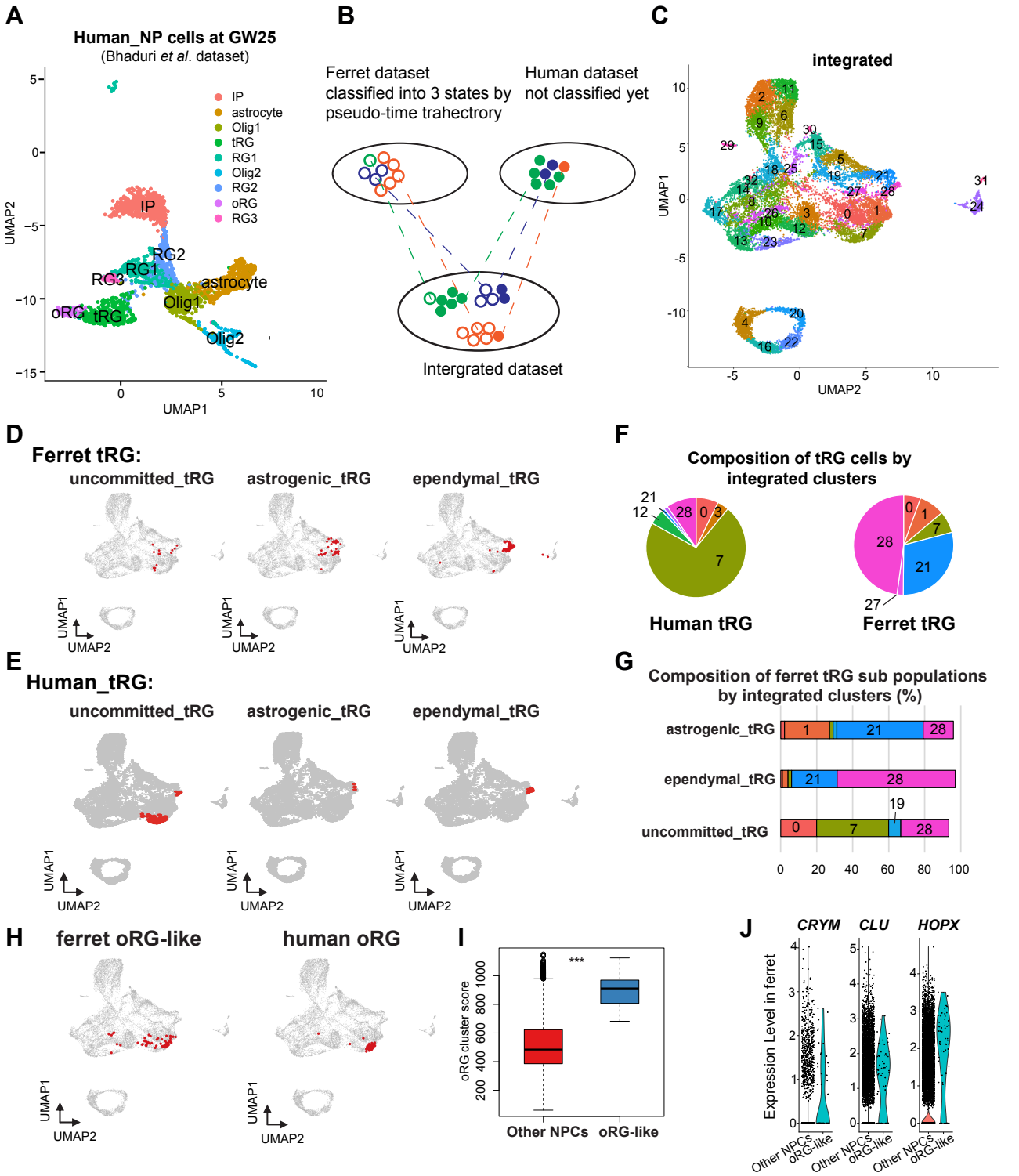

Figure S1. Development of the ferret cerebral cortex.

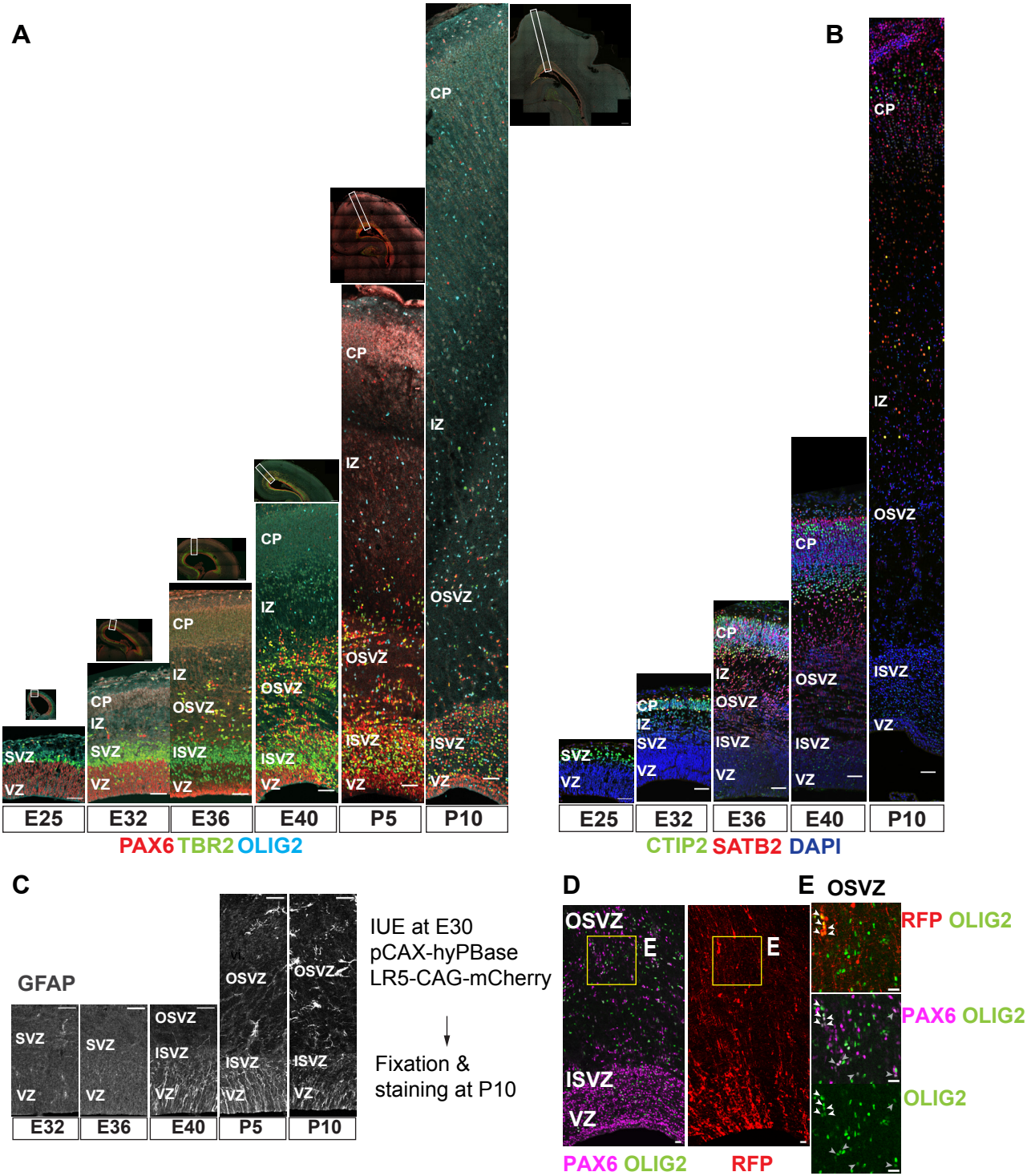

Fig. S2 Quality and reproducibility in ferret sc transcriptomes

A. Cortical regions used for scRNA-sq

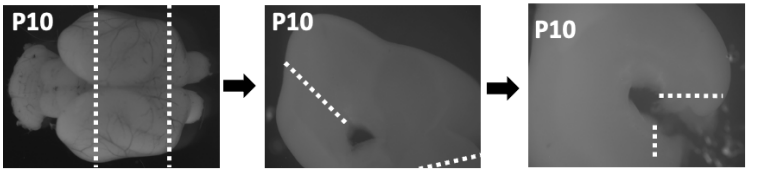

removal of the posterior and anterior sides

removal of the medial cortex and ventral telencephalon

B. Two different preparations of cortical cells give nearly identical results.

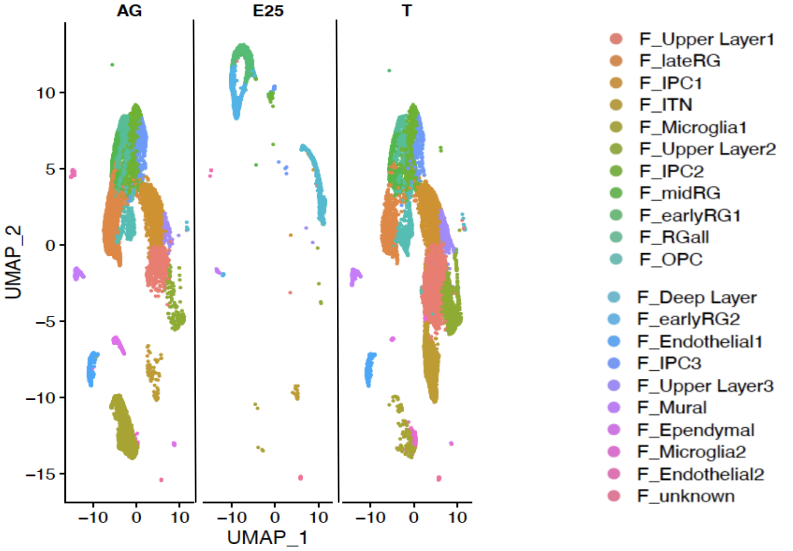

C. Two different cut off levels of mitochondoria contents give nearly identical results.

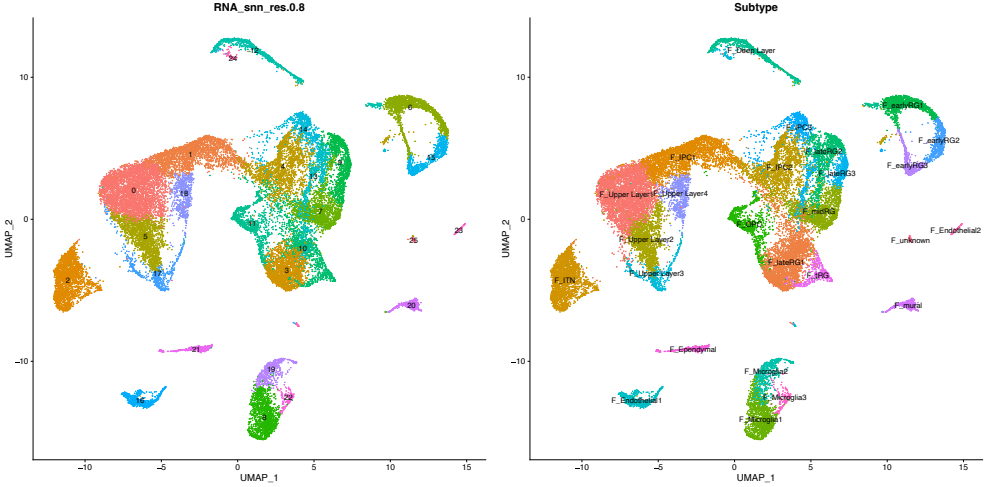

Figure S3. Cell types in developing ferret cerebral cortex.

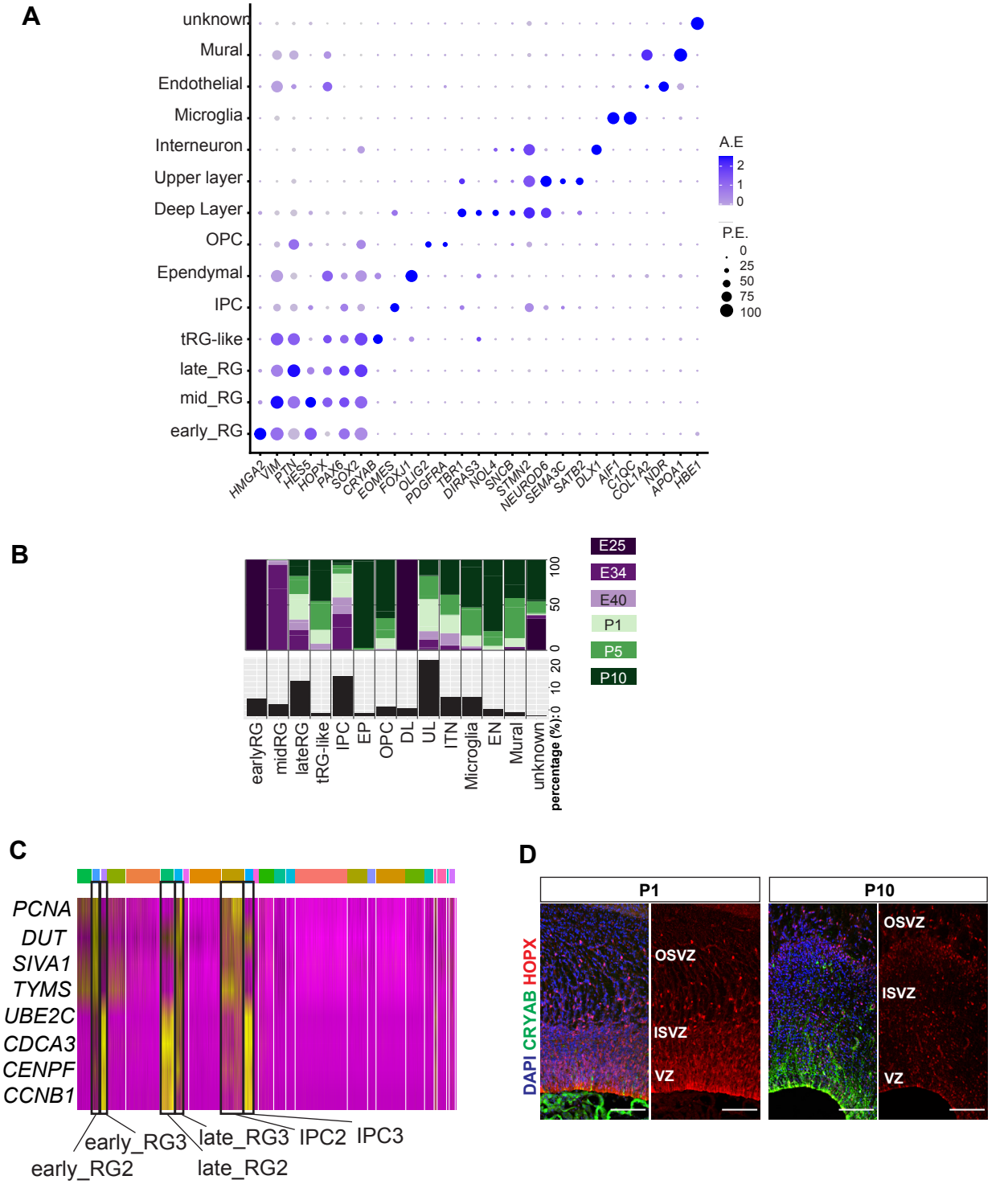

Figure S4. Development of ferret tRG during post-natal cortical development.

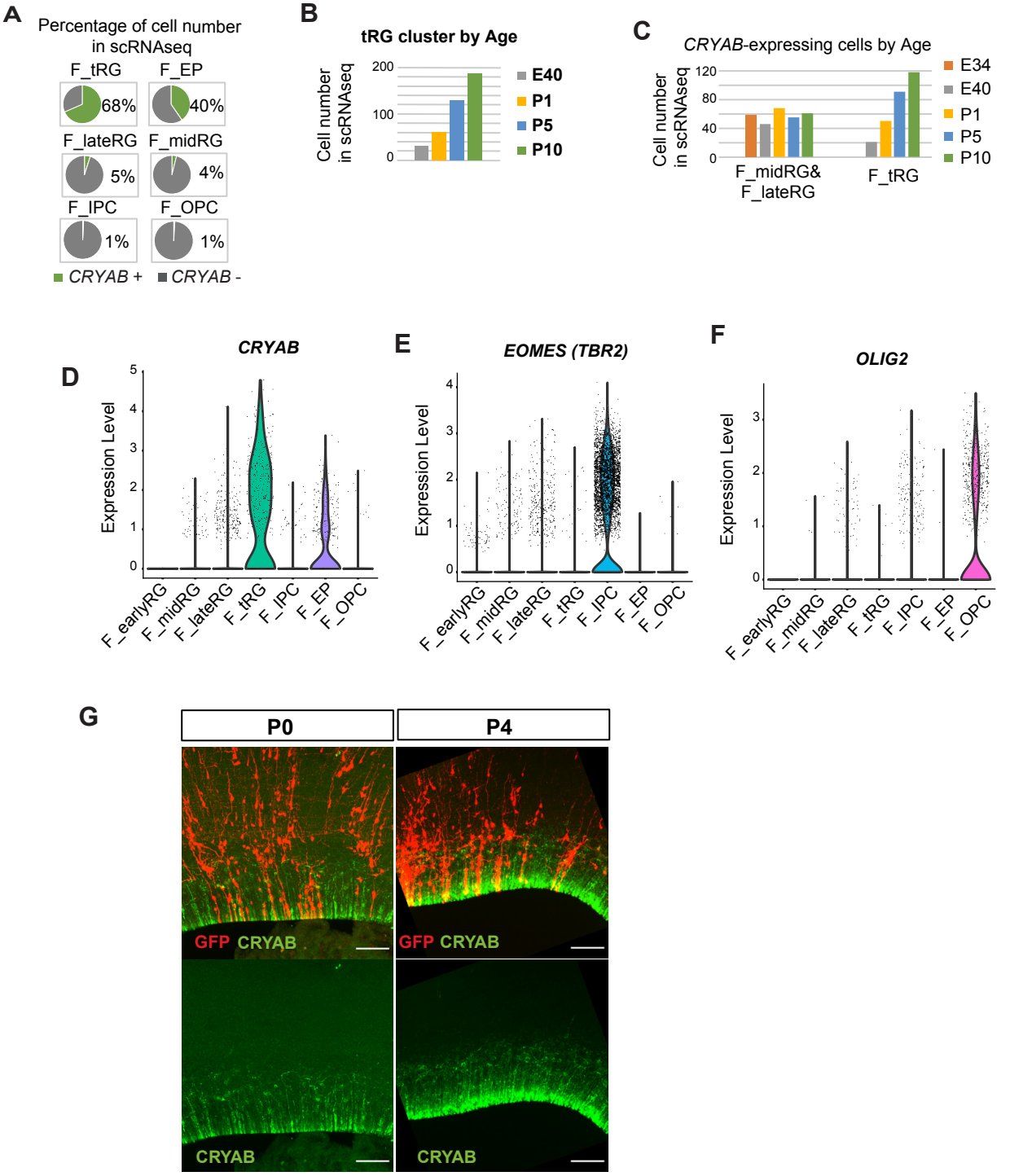

Figure S5. Temporal fates of RG cells predicted by pseudo-time trajectory analysis.

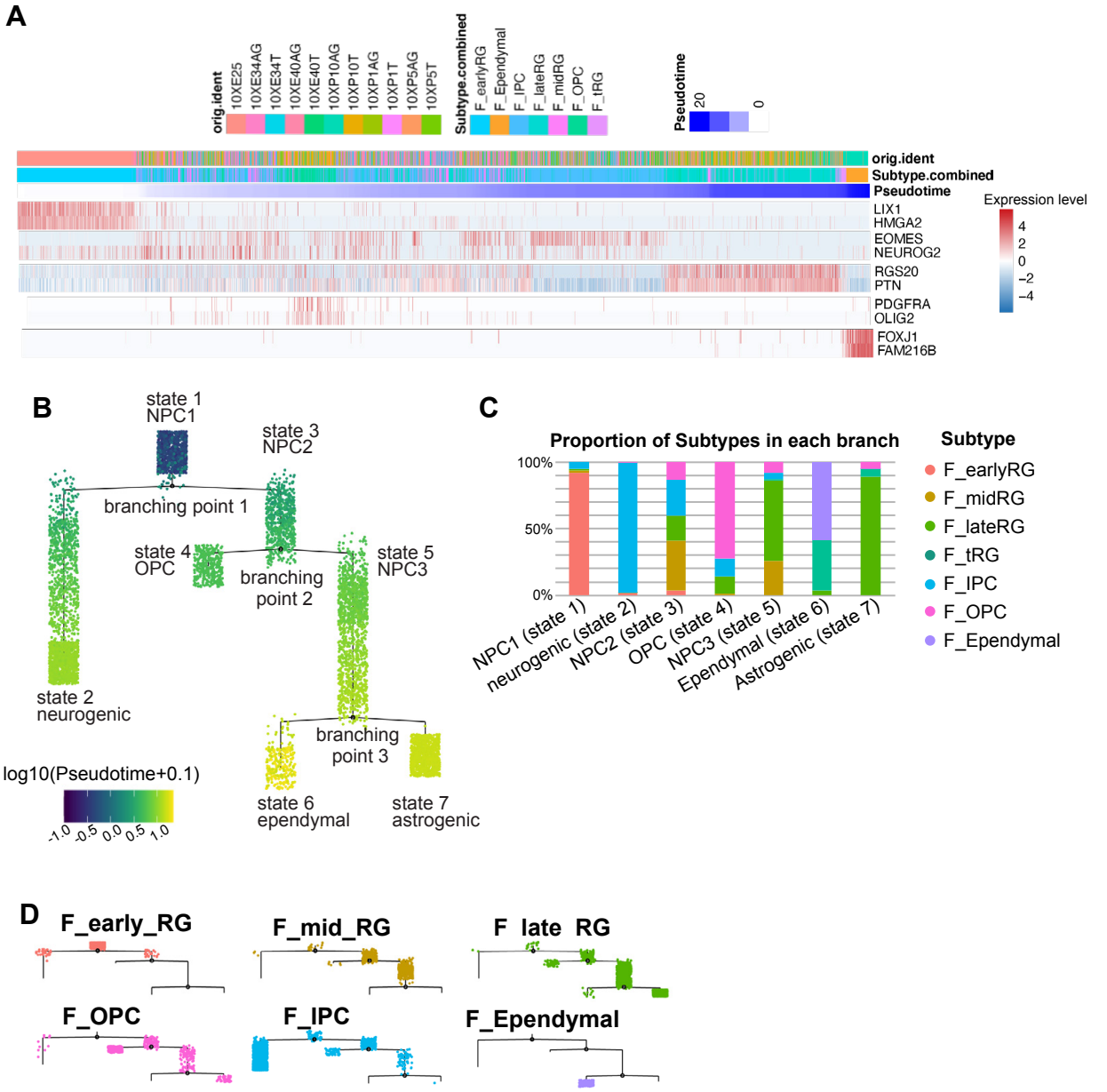

Figure S6. tRG adopt both ependymal and astrogenic fates in ferrets.

A

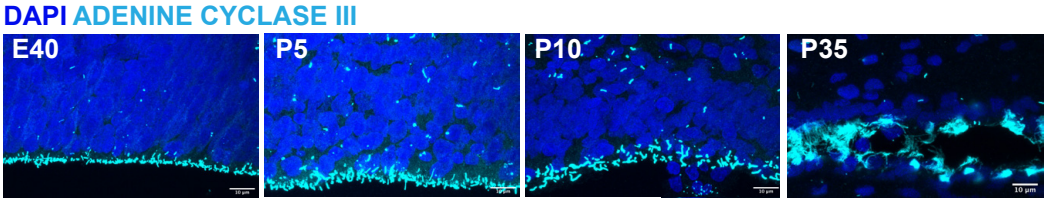

B

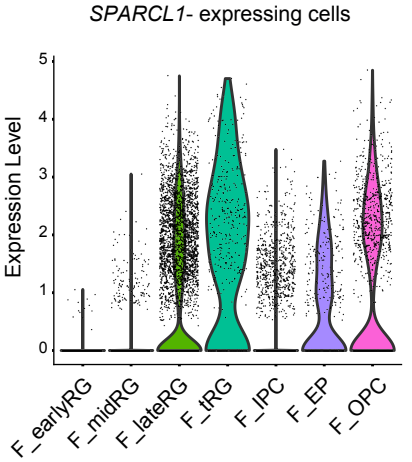

C

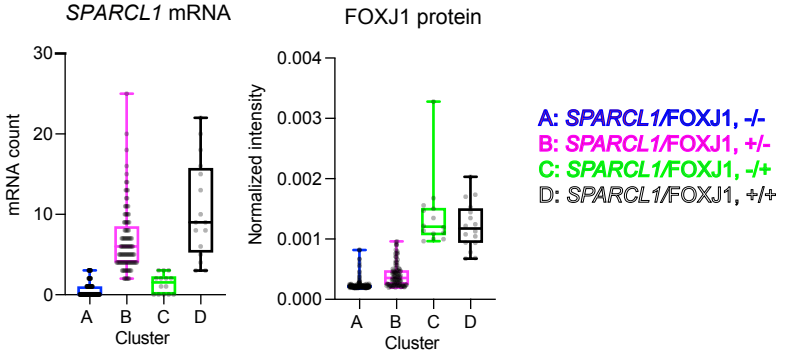

D

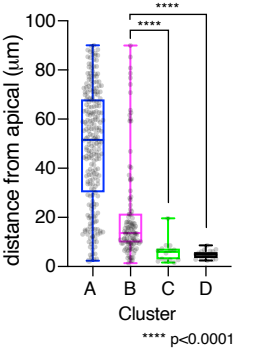

Figure S7. Comparison of molecular identity of RG subtypes between ferret and human.

A

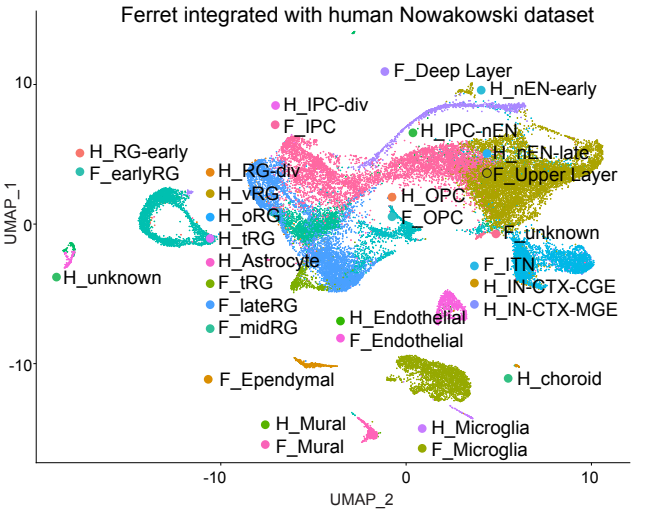

B

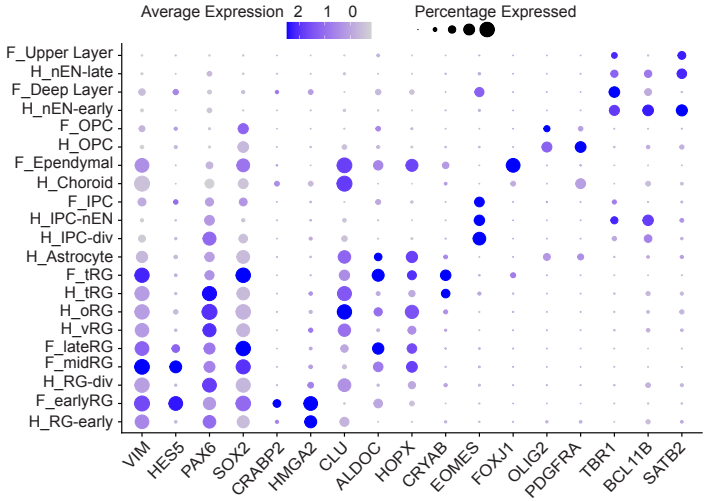

Figure S8. Comparison of the tRG and oRG subtypes between ferrets and humans.

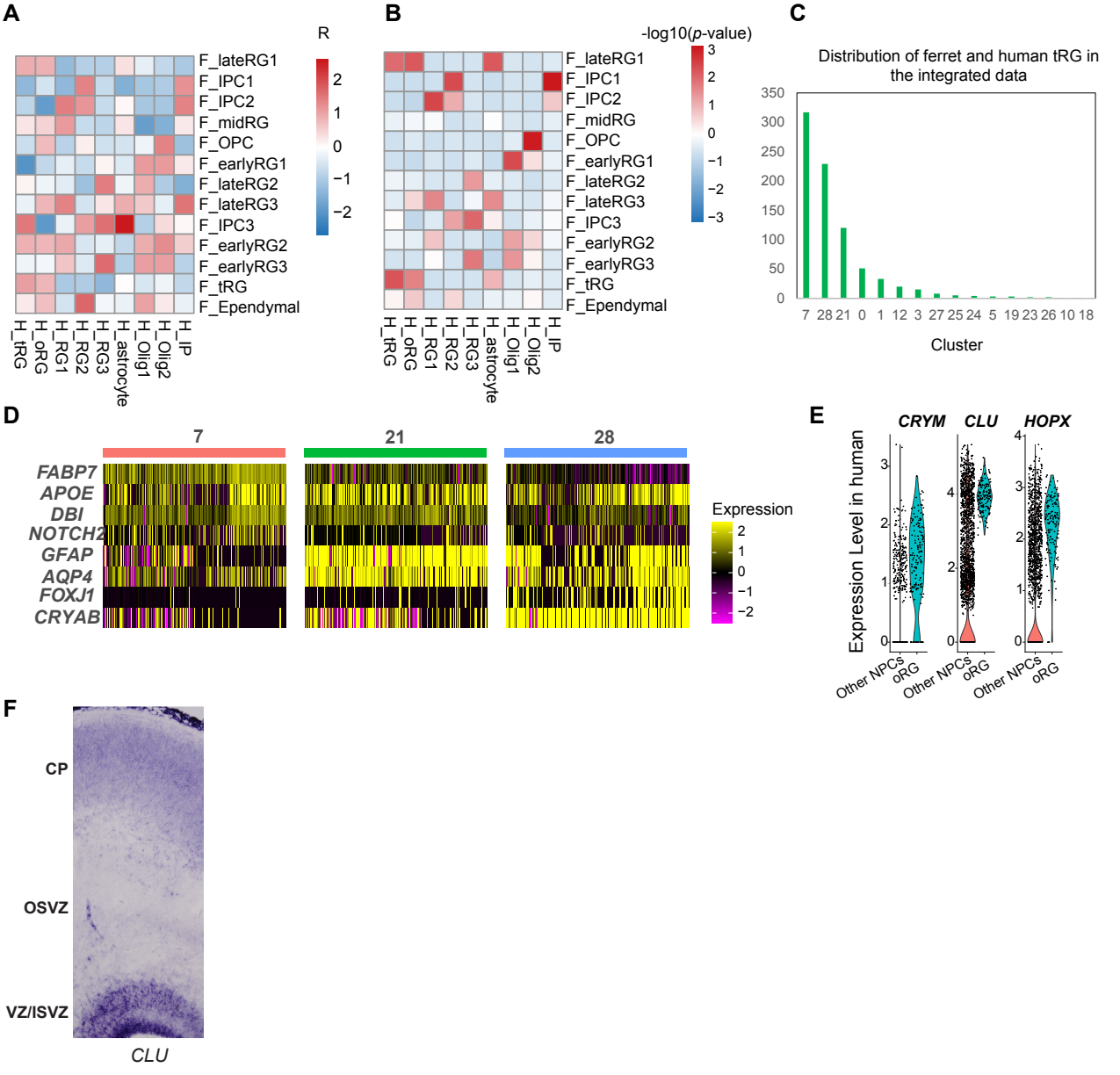
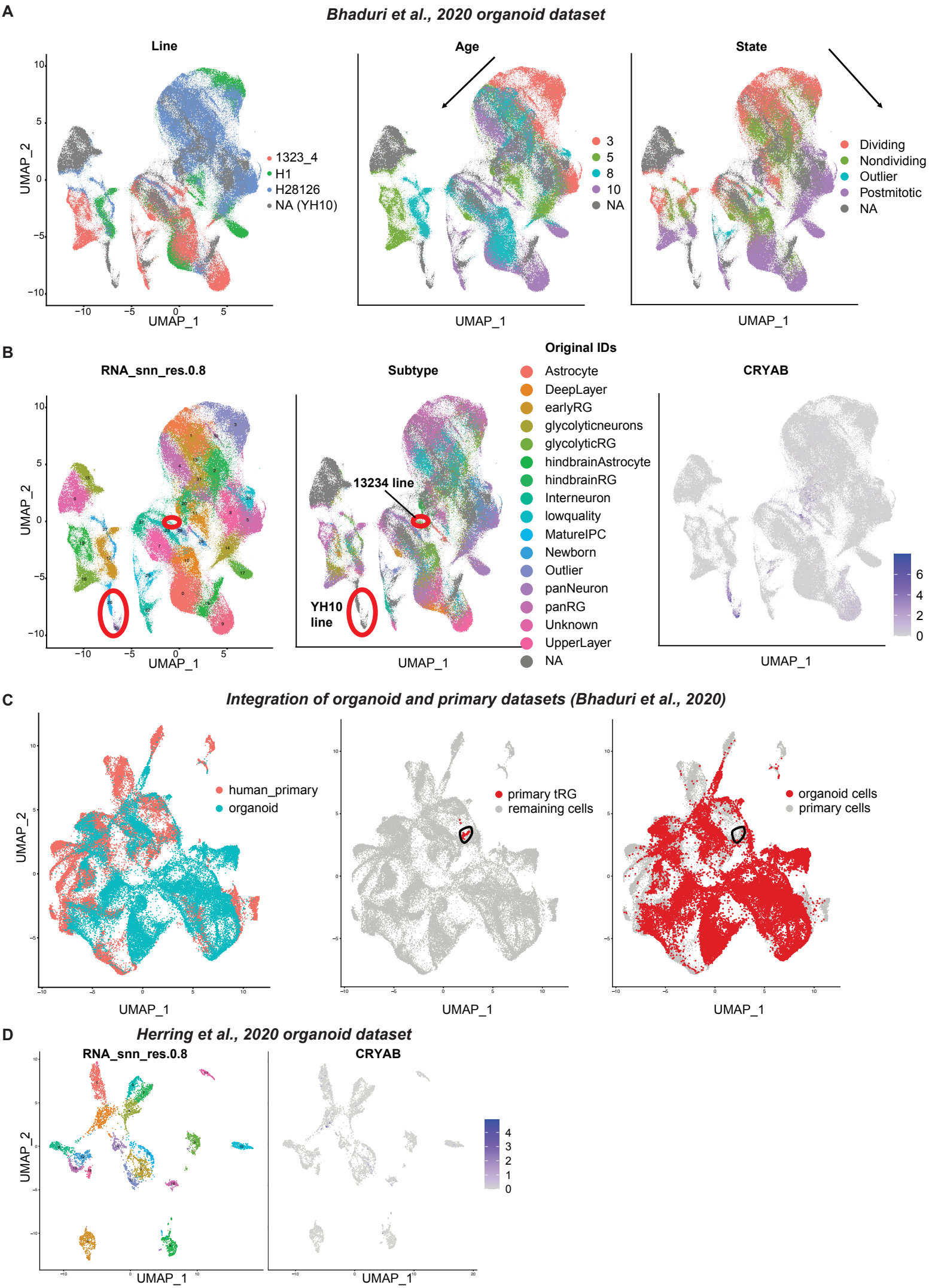
Figure S9. Single cell analysis of cortical organoid dataset.